ChemPubSoc Europe
DOI: 10.1002/chem.201603640
CHEMISTRY
A European Journal
Full Paper

Single-Molecule Magnets

Observation of Slow Relaxation and Single-Molecule Toroidal Behavior in a Family of Butterfly-Shaped Ln_4 Complexes

Sourav Biswas,[a] Sourav Das,[b] Tulika Gupta,[c] Saurabh Kumar Singh,[d] Michael Pissas,[e]
Gopalan Rajaraman,*[c] and Vadapalli Chandrasekhar*[a, f]

Abstract: A family of five isostructural butterfly complexes with a tetranuclear $[Ln_4]$ core of the general formula $[Ln_4(LH)_2(\mu_2\text{-}\eta^1\eta^1Piv)(\eta^2\text{-}Piv)(\mu_3\text{-}OH)_2]\cdot x\,H_2O\cdot y\,MeOH\cdot z\,CHCl_3$ (**1**: Ln = Dy^{III}, $x=2$, $y=2$, $z=0$; **2**: Ln = Tb^{III}, $x=0$, $y=0$, $z=6$; **3**: Ln = Er^{III}, $x=2$, $y=2$, $z=0$; **4**: Ln = Ho^{III}, $x=2$, $y=2$, $z=0$; **5**: Ln = Yb^{III}, $x=2$, $y=2$, $z=0$; LH_4 = 6-{[bis(2-hydroxyethyl)amino]methyl}-*N′*-(2-hydroxy-3-methoxybenzylidene)picolinohydrazide; PivH = pivalic acid) was isolated and characterized both structurally and magnetically. Complexes **1**–**5** were probed by direct and alternating current (dc and ac) magnetic susceptibility measurements and, except for **1**, they did not display single-molecule magnetism (SMM) behavior. The ac magnetic susceptibility measurements show frequency-dependent out-of-phase signals with one relaxation process for complex **1** and the estimated effective energy barrier for the relaxation process was found to be 49 K. We have carried out extensive ab initio (CASSCF + RASSI-SO + SINGLE_ANISO + POLY_ANISO) calculations on all the five complexes to gain deeper insights into the nature of magnetic anisotropy and the presence and absence of slow relaxation in these complexes. Our calculations yield three different exchange coupling for these Ln_4 complexes and all the extracted *J* values are found to be weakly ferro/antiferromagentic in nature ($J_1=+2.35$, $J_2=-0.58$, and $J_3=-0.29\ cm^{-1}$ for **1**; $J_1=+0.45$, $J_2=-0.68$, and $J_3=-0.29\ cm^{-1}$ for **2**; $J_1=+0.03$, $J_2=-0.98$, and $J_3=-0.19\ cm^{-1}$ for **3**; $J_1=+4.15$, $J_2=-0.23$, and $J_3=-0.54\ cm^{-1}$ for **4** and $J_1=+0.15$, $J_2=-0.28$, and $J_3=-1.18\ cm^{-1}$ for **5**). Our calculations reveal the presence of very large mixed toroidal moment in complex **1** and this is essentially due to the specific exchange topology present in this cluster. Our calculations also suggest presence of single-molecule toroics (SMTs) in complex **2**. For complexes **3**–**5** on the other hand, the transverse anisotropy was computed to be large, leading to the absence of slow relaxation of magnetization. As the magnetic field produced by SMTs decays faster than the normal spin moments, the concept of SMTs can be exploited to build qubits in which less interference and dense packing are possible. Our systematic study on these series of Ln_4 complexes suggest how the ligand design can help to bring forth such SMT characteristics in lanthanide complexes.

Introduction

Research on lanthanide-ion-based molecular magnetic materials is a fast developing area.[1] Since the seminal discovery of single-molecule magnet (SMM) behavior in $Mn_{12}O_{12}(OAc)_{16}(H_2O)_4]\cdot 2\,HOAc\cdot 4\,H_2O$[2] this field has expanded to single-chain magnets,[3] and single-ion magnets.[3b,4] Although initially polynuclear complexes containing 3d[5] metal ions were being investigated for SMM behavior, very soon 3d/4f heterometallic complexes[6] and subsequently homometallic 4f[7,9] complexes have been found suitable for SMM applications. In particular, complexes containing Dy^{III}, Tb^{III}, and Ho^{III} have been

---

[a] S. Biswas, Prof. V. Chandrasekhar
Department of Chemistry, Indian Institute of Technology Kanpur
Kanpur 208016 (India)
E-mail: vc@iitk.ac.in

[b] Dr. S. Das
Department Of Chemistry
Institute of Infrastructure Technology Research and Management
Near Khokhara Circle, Maninagar East, Ahmedabad 380026 (India)

[c] T. Gupta, Dr. G. Rajaraman
Department of Chemistry, Indian Institute of Technology Bombay
Powai, Mumbai 400076 (India)
E-mail: rajaraman@chem.iitb.ac.in

[d] Dr. S. K. Singh
Department of Molecular Theory and Spectroscopy
Max-Planck Institute for Chemical Energy Conversion
Stiftstr 34-36, 45470 Mülheim an der Ruhr (Germany)

[e] Dr. M. Pissas
Institute of Advanced Materials, Physicochemical Processes
Nanotechnology and Microsystems
NCSR Demokritos, 15310 Ag. Paraskevi, Attiki, (Greece)

[f] Prof. V. Chandrasekhar
National Institute of Science Education and Research
Institute of Physics Campus, Sachivalaya Marg, PO: Sainik School
Bhubaneswar 751 005, Orissa (India)

*Supporting information for this article can be found under http://dx.doi.org/10.1002/chem.201603640. It contains the molecular structures of **2**–**5** (Figures S1–S4), list of bond length and bond angles (Tables S1–S4), literature reported butterfly shaped complexes, CASSCF + RASSI-SO + SINGLE_ANISO computed energies, SINGLE_ANISO computed crystal field parameters of **1**–**5** (Tables S5–14), angle between main anisotropy axes (Table S15) of **1**, temperature dependence of the a) in-phase and b) out-of-phase ac susceptibility plot of **1** (Figure S6).*

investigated extensively, since these ions possess a relatively high ground state spin along with significant unquenched orbital angular momentum. These two parameters are important in generating energy barriers for the reversal of magnetization. Among the homometallic lanthanide ion complexes, the tetranuclear family offers considerable structural diversity and varied structural topologies such as linear,[8] distorted cubane,[9] square-grid,[10] tetrahedron,[11] trigonal pyramid,[12] zig-zag,[13] butterfly[14a–l] rhombus,[15] and irregular (Y-shaped,[16] ladder type,[17] sea-saw[18]) are known. This family also contains some examples such as $[Dy_4K_2O(OtBu)_{12}]$[12] and $[Dy_4(\mu_3\text{-}OH)_2(bmh)_2(msh)_4Cl_2]$[14g] (bmh = 1,2-bis(2-hydroxy-3-methoxybenzylidene) hydrazone; msh = methoxysalicy-laldehyde hydrazone) which showed very high energy barriers for magnetization reversal. Recently, a review summarizing the SMM behavior of tetranuclear Dy^{III} family has appeared.[1d]

In addition to SMM behavior, in recent years, the importance of single-molecule toroics (SMTs)[15] is becoming important. The electromagnetic response of a toroidal arrangement of magnetic moments in complexes has several potential applications.[16] Toroidal moments[17] in SMTs are expected to arise from wheel-shaped vortex arrangements of local magnetic moments and are essentially governed by magnetic exchange interaction between the metal centers. Besides, the toroidal magnetic states are promising for building quantum computing and information storage as they are insensitive to homogeneous magnetic fields.[16–18] This renders a more protective environment (with respect to the application of magnetic field) to the two components of the toroidal magnetic state and the respective circular arrangement of magnetic moments in reverse directions[17b] (in comparison with spin-projected eigenstates of true spin $S = 1/2$).[18] Moreover, since the magnetic field produced by a net toroidal moment decays much faster than the field of a normal magnetic dipole, qubits designed[18a] on the basis of toroidal moments will be much less interfering and, therefore, could be packed much more densely than spin qubits.[18a] Also, the toroidal magnetic moment interacts with a dc current passing through the molecule[19] or a time-varying electric field[20] by means of magneto-electric coupling[21] and this allows the moment to be controlled and manipulated purely by electrical means, a property much sought after in molecular devices.[18a] Despite these features, the number of molecules exhibiting toroidal moments are relatively small, as concrete efforts to control the direction of the anisotropic axes is needed to achieve toroidal moments at the ground state.

Another aspect that remains intriguing among lanthanide complexes is that the underlying complexity of the ligand field environment around Ln^{III} ions complicates a precise estimation of the anisotropic axes of these complexes. Though various experimental tools, that is, inelastic neutron scattering,[22] multi-frequency high-field EPR,[23] field- and orientation-dependent magnetic susceptibility, have been utilized to probe the magnetic anisotropy,[24] precise estimation of the directions of local anisotropy axes remains, nevertheless, challenging. This can be remedied by fragment quantum chemistry calculations, accounting for spin-orbit coupling in a non-perturbative manner. Despite difficulties in analyzing the single-ion nature of core-like 4f orbitals of Ln^{III} ions, significant progress in the post Hartree–Fock multiconfigurational ab initio methodology has been achieved towards resolving these issues. The CASSCF + RASSI-SO + SINGLE_ANISO[25] approach has been employed to depict the magnetic properties of individual metal ions. This can be followed by the estimation of anisotropic interaction between the Ln^{III} sites within the Lines model as implemented in the POLY_ANISO code.[26]

Our laboratory has been investigating the tetranuclear lanthanide ion complex family.[7g,9,27] Thus, we have reported cubane-shaped $[Ln_4(L)_4(\mu_2\text{-}\eta^1\eta^1Piv)_4]$ (LH_2 = 2-{[6-(hydroxymethyl)pyridin-2-yl]methyleneamino}phenol)[9] and rhombus-shaped complexes, $[Ln_4(LH)_2(\mu_2\text{-}O)_2(H_2O)_8]$[27a] ($LH_3$ = (6-hydroxymethyl)-*N*′-[(8-hydroxyquinolin-2-yl)methylene]picolinohydrazide). Interestingly the Dy^{III} analogue of both of these families shows two relaxation pathways in their ac susceptibility studies. Recently we were also able to prepare $[Ln_4(L)_4(\mu_4\text{-}OH)(\mu_3\text{-}OH)_2(NO_3)_4]$[7g] (LH = 2-methoxy-6-(pyridin-2-ylhydrazonomethyl)phenol) with a see-saw topology and $[Ln_4(LH)_2(LH_2)_2(\mu_2\text{-}\eta^1\eta^1Piv)_2(\eta^1\text{-}Piv)_4]$ (LH_3 = *N*′-(2-hydroxy-3-methoxybenzylidene)-6-(hydroxymethyl)picolinohydrazide}),[27b] which contains two dimeric subunits.

Motivated by these results, we designed a new flexible compartmental aroyl hydrazone ligand, 6-{[bis(2-hydroxyethyl)amino]methyl}-*N*′-(2-hydroxy-3-methoxybenzylidene)picolinohydrazide (LH_4), which upon reaction with $Ln(NO_3)_3\cdot 5H_2O$ (Ln = Dy, Tb, Er, Ho and Yb) afforded butterfly-shaped homometallic tetranuclear complexes $[Ln_4(LH)_2(\mu_2\text{-}\eta^1\eta^1Piv)(\eta^2\text{-}Piv)(\mu_3\text{-}OH)_2]\cdot x H_2O\cdot y MeOH\cdot z CHCl_3$ (**1**: Ln = Dy^{III}, $x = 2$, $y = 2$, $z = 0$; **2**: Ln = Tb^{III}, $x = 0$, $y = 0$, $z = 6$; **3**: Ln = Er^{III}, $x = 2$, $y = 2$, $z = 0$; **4**: Ln = Ho^{III}, $x = 2$, $y = 2$, $z = 0$; **5**: Ln = Yb^{III}, $x = 2$, $y = 2$, $z = 0$) (Scheme 1). The synthesis, structure and magnetism of **1–5** are described herein, along with detailed theoretical studies on these complexes.

Result and Discussion

Synthetic aspects

Multidentate ligands containing various functional groups (carboxylate, hydroxyl, oxime, methoxy, ethoxy and amine) have been employed to construct polynuclear lanthanide complexes.[7g,9,14,27] Among these, multidentate, flexible aroylhydrazone-based Schiff base ligands appear to be very promising. First, these ligands can display keto–enol tautomerism, in which both the isomeric forms of the ligand are anticipated to exhibit different binding modes to the metal centers depending upon the conditions. Second, C–C bond rotation (conformational isomers)[7a,27b,28] in these ligands opens up an additional source of coordination flexibility. Utilizing these characteristics in *N*′-(2-hydroxy-3-methoxybenzylidene)-6-(hydroxymethyl)picolinohydrazide (LH_3), we have previously assembled Ln_4 and Ln_6 complexes (Scheme 2).

In order to introduce further versatility in the above ligand system, we have prepared 6-{[bis(2-hydroxyethyl)amino]methyl}-*N*′-(2-hydroxy-3-methoxybenzylidene)picolinohydrazide (LH_4), which is similar to LH_3 except that the pendent $-CH_2OH$

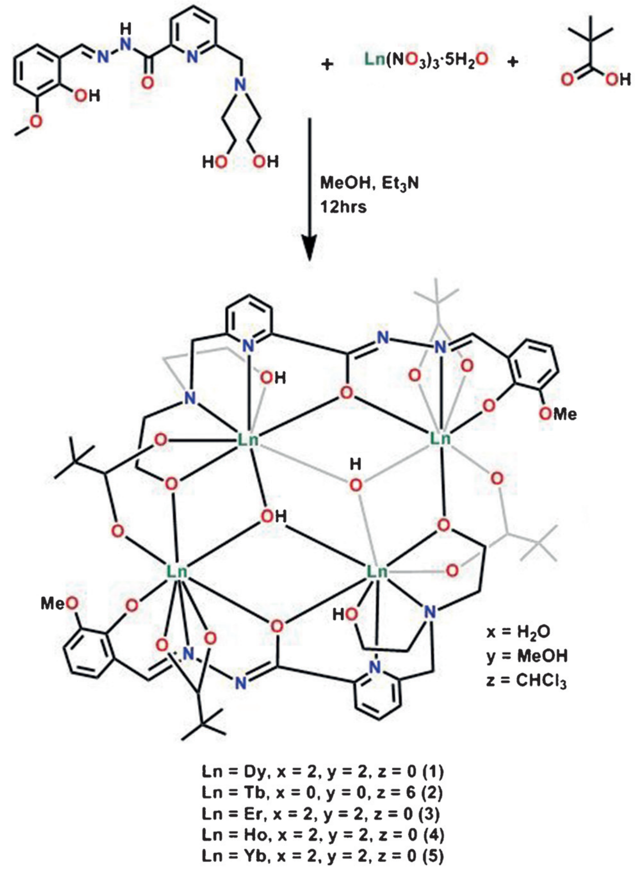

Scheme 1. Synthesis of tetrametallic Ln_4 complexes **1**–**5**.

in the latter is replaced by the $-[CH_2N(CH_2CH_2OH)_2]$ motif. The choice of pendent was dictated by the knowledge that while the $-CH_2CH_2OH$ arm acts as a chelating ligand (along with the nitrogen), in its deprotonated form it acts as a bridging ligand. LH_4 was synthesized by following a five-step synthetic protocol (Scheme 3). LH_4 contains eight potential coordinating sites with two unsymmetrical pockets: one of these is tetradentate and consists of a methoxy, a hydroxy, an imine nitrogen and an enolized hydrazone oxygen atom, while the other is pentadentate and possesses a diethanol amine, a pyridine nitrogen, and a common enolizable oxygen atom (Figure 1). The reaction of LH_4 with the $Ln(NO_3)_3{\cdot}5H_2O$ and pivalic acid in the pres-

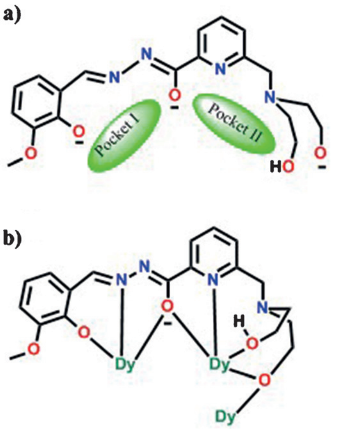

Figure 1. a) The two coordinating pockets of $[LH]^{3-}$ in its enolized form. b) Coordination mode of the ligand $[LH]^{3-}$.

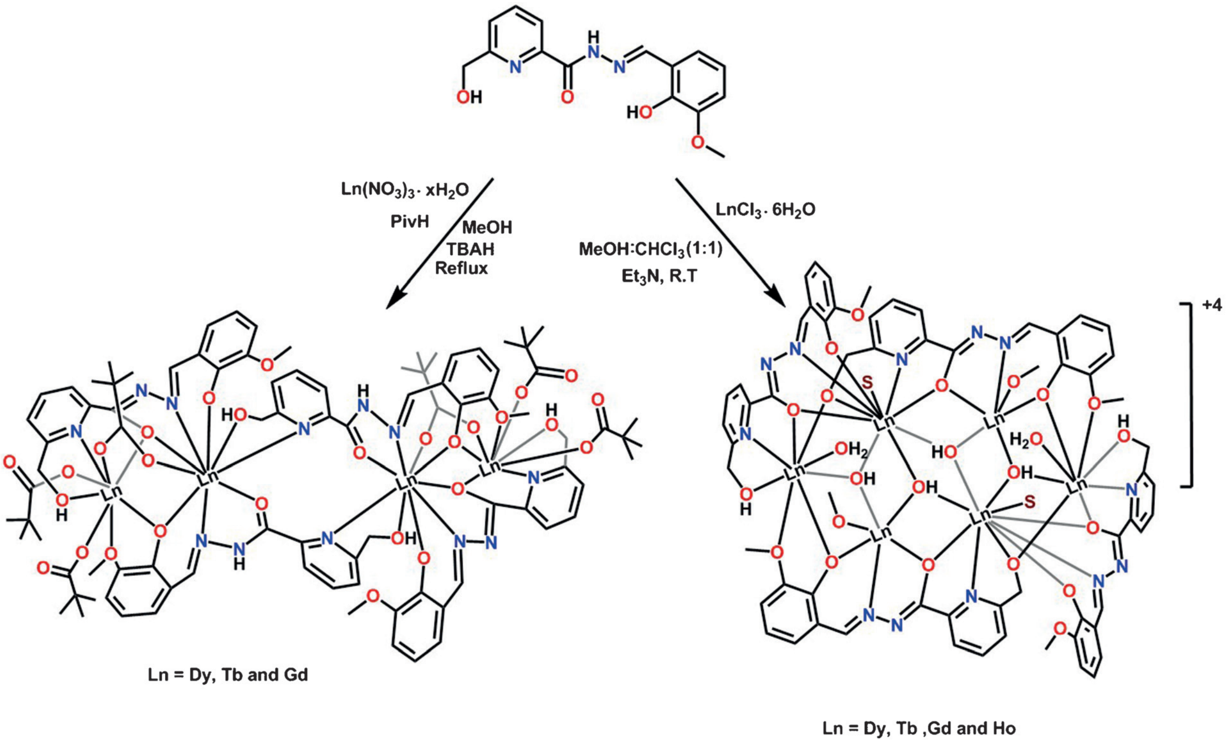

Scheme 2. a) A Ln_4 complex containing both keto and enol forms of the ligand.[27b] b) A Ln_6 complex containing only the enol form of the ligand.[7a]

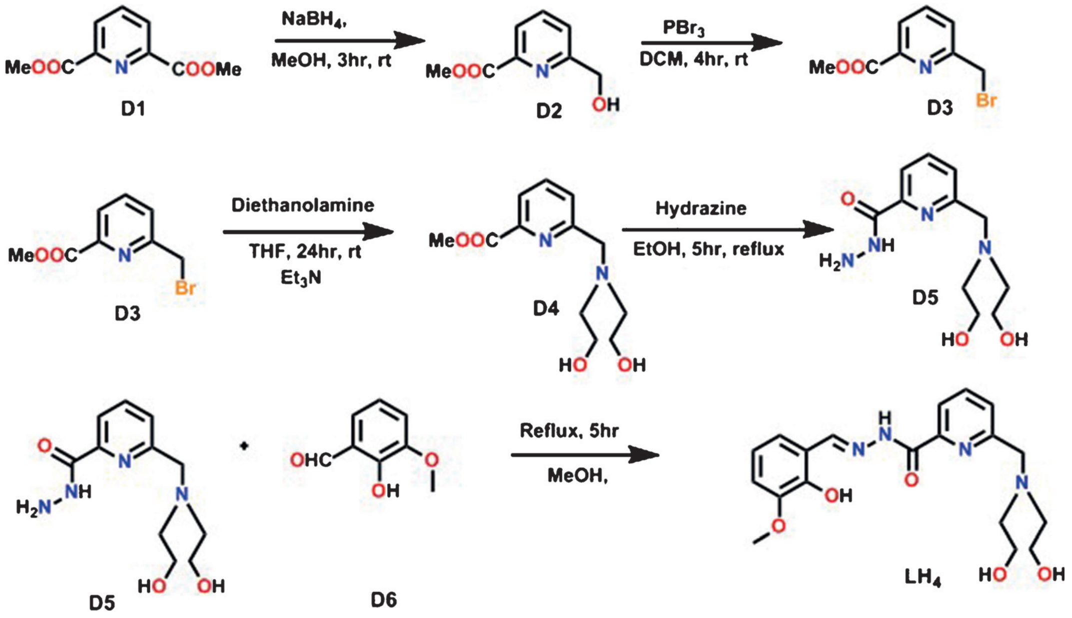

Scheme 3. Synthesis of the ligand LH_4.

ence of triethylamine as a base (1:2:2:5) afforded butterfly-shaped homometallic tetranuclear complexes, $[Ln_4(LH)_2(\mu_2\text{-}\eta^1\eta^1\text{Piv})(\eta^2\text{-Piv})(\mu_3\text{-OH})_2]\cdot x\,H_2O\cdot y\,MeOH\cdot z\,CHCl_3$ (**1**: Ln = Dy^{III}, $x=2$, $y=2$, $z=0$; **2**: Ln = Tb^{III}, $x=0$, $y=0$, $z=6$; **3**: Ln = Er^{III}, $x=2$, $y=2$, $z=0$; **4**: Ln = Ho^{III}, $x=2$, $y=2$, $z=0$; **5**: Ln = Yb^{III}, $x=2$, $y=2$, $z=0$) (Scheme 1).

X-ray crystal structures of 1–5

Single-crystal X-ray diffraction studies reveal that compounds **1**, **3**, **4** and **5** crystallize in the monoclinic system in space group $P2_1/n$ with $Z=2$. Compound **2** crystallizes in the space group $P2_1/c$. Although the asymmetric units of **1–5** contain half of the total molecule, their structural motifs are not identical: **1** possess a $[Dy_2(LH)(\mu_2\text{-}\eta^1\eta^1\text{Piv})(\eta^2\text{-Piv})(OH)]$ motif (Figure 2a), while **2–5** possess $[Ln_2(LH)(\eta^2\text{-Piv})(\eta^1\text{-Piv})(\mu_2\text{-OH})]$ motifs. All the compounds are neutral and possess the same structural topology with a butterfly-shaped tetrametallic core. In view of their similarity, compound **1** has been chosen as a representative example to describe the structural features of this family of complexes. Selected bond parameters of **1** are given in Table 1. The molecular structures and selected bond parameters of **2–5** are given in the Supporting Information (Figure S1–S4 and Tables S1–S4). A perspective view of the molecular structure of **1** is portrayed in Figure 2b.

The homometallic tetranuclear complex $[Ln_4(LH)_2(\mu_2\text{-}\eta^1\eta^1\text{Piv})_2(\eta^2\text{-Piv})_2(\mu_3\text{-OH})_2]$ is formed by the cumulative coordination action of two triply deprotonated ligands, $[LH]^{3-}$ along with four pivalate ligands. Although the ligand LH_4 contains nine potential coordinating sites, only seven of these are involved in assembling the tetranuclear complex. The other two, namely, the OMe group and the hydrazine nitrogen (near the carbonyl carbon) do not participate in binding. Within complex **1**, it has been found that each ligand can accommodate the two Dy^{III} ions simultaneously in its two multidentate flexible pockets [pentadentate (OONNO) and tridentate (ONO)] (Figure 1a). Both the metal centers within the pockets of $[LH]^{3-}$ are effectively linked by the enolized hydrazone oxygen. Each

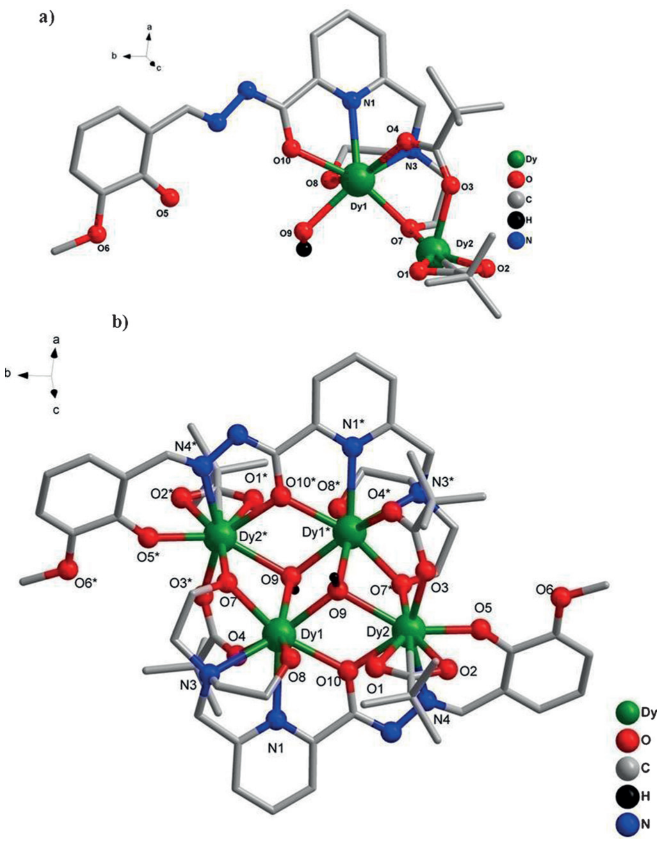

Figure 2. a) Asymmetric unit of **1**. b) Molecular structure of **1** (selected hydrogen atoms and the solvent molecules have been omitted for clarity).

Table 1. Selected bond lengths [Å] and bond angle [°] parameters of **1**.

Bond lengths around Dy1		Bond lengths around Dy 2		Bond angles around Dy	
Dy1—O7	2.259(2)	Dy2—O5	2.216(2)	Dy1-O10-Dy2*	113.68(10)
Dy1—O4	2.314(2)	Dy2—O7	2.272(2)	Dy1-O7-Dy2	108.57(10)
Dy1—O9	2.340(3)	Dy2—O3	2.305(3)	Dy1-O9-Dy1[a]	108.35(10)
Dy1—O10	2.348(2)	Dy2—O10*	2.358(2)	Dy1-O9-Dy2[a]	110.26(10)
Dy1—O9[a]	2.353(2)	Dy2—O1	2.432(3)	Dy1[a]-O9-Dy2[a]	99.61(9)
Dy1—O8	2.409(3)	Dy2—O9*	2.462(2)		
Dy1—N1	2.520(3)	Dy2—N4	2.518(3)		
Dy1—N3	2.641(3)	Dy2—O2	2.521(3)		

[a] Atoms are generated by the symmetry operation *: 0.5−*x*, 0.5+*y*, 0.5−*z*.

pentadentate pocket of two $[LH]^{3-}$ contains two ethanolamine arms. One of these is neutral and functions as a chelating ligand, while the other is de-protonated and acts as a bridging ligand (μ-O) between two metal centers connecting the two Dy_2 sub-units. In addition to the binding provided by the ligand $[LH]^{3-}$, the tetranuclear ensemble is further strengthened by two μ_3-OH ligands and four pivalate ions; two of these are chelating (η^2) while the other two are bridging (μ_2-η^1:η^1). Thus, overall, each $[LH]^{3-}$ adopts a μ_3-η^1:η^2:η^1:η^2:η^1:η^1 coordination mode (Figure 1 b) and, along with four pivalate and two μ_3-OH groups, enables the construction of the butterfly-shaped tetranuclear core, $[Dy_4(\mu_2\text{-}O)_4(\mu_2\text{-}OH)_2]^{6+}$ (Figure 3). This core contains four coplanar Dy^{III} centers, Dy1 and Dy1* represent the central region, while Dy2 and Dy2* represent the wing-tips.

Further analysis of the core of the complex **1** reveals some interesting structural features. The central core $[Dy_4(\mu_3\text{-}OH)_2]^{10+}$ can be expanded to two edge-sharing triangular units (Dy1-Dy2-Dy1* and Dy1-Dy1*-Dy2*). One face of each triangular unit is capped by a μ_3-OH ligand.

Overall, **1** contains two structurally distinct eight-coordinated Dy^{III} ions with distorted triangular dodecahedron geometries; one of them possesses a 7O, 1N coordination environment (Figure 4 a), while the other has a 6O, 2N coordination environment (Figure 4 b). Among the three Dy-μ_3-OH bonds two are significantly shorter (2.338, 2.351 Å) than the other (2.458 Å). Among the other Dy—O distances, those involving Dy—O_{phen} (2.216 Å) are the shortest. The average Dy⋯Dy distance is 4.274 Å (shortest distance being 3.678 Å, largest distance, 6.606 Å).

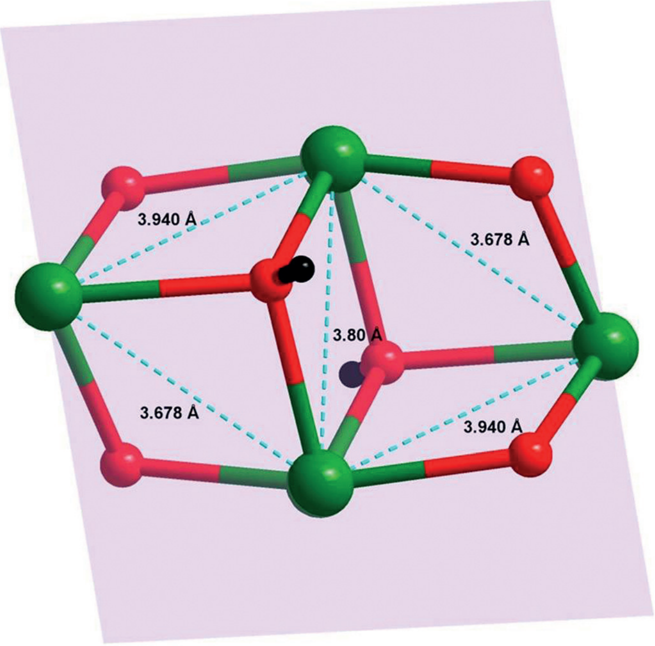

Figure 3. Butterfly-shaped core containing two triangular units and two defect-cubane units.

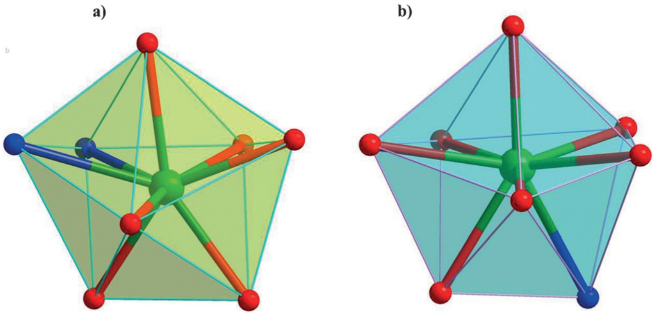

Figure 4. a) Distorted triangular dodecahedral geometry containing 6O, 2N. b) Distorted triangular dodecahedral geometry containing 7O, 1N.

The butterfly-shaped core topology observed in the present instance has been seen earlier, but the preparation of such complexes has involved different ligand systems (Supporting Information). A comparison of the structural and magnetic properties of the butterfly-shaped tetranuclear lanthanide complexes is listed in Table 2.

Magnetic studies

The direct-current (dc) magnetic susceptibility measurements of complexes **1**–**5** were performed in the 2–300 K temperature range and under an applied magnetic field of 0.1 or 1 T (Figures 5 and 6). The room-temperature $\chi_M T$ values (56.51, 46.44, 44.45, 55.52 and 9.52 $cm^3\,K\,mol^{-1}$, for **1**–**5**, respectively) are close to the calculated values of 56.68, 47.25, 45.90, 56.25 and 10.29 $cm^3\,K\,mol^{-1}$ for the ground state of the four magnetically non-interacting Dy^{III} ions ($4f^9$, $J=15/2$, $S=5/2$, $L=5$, $g=4/3$; $^6H_{15/2}$), Tb^{III} ions ($4f^8$, $J=6$, $S=3$, $L=3$, $g=3/2$; $^7F_6$), Er^{III} ions ($4f^{11}$, $J=15/2$, $S=3/2$, $L=6$, $g=6/5$; $^4I_{15/2}$), Ho^{III} ions ($4f^{10}$, $J=8$, $S=2$, $L=6$, $g=5/4$; $^5I_8$) and Yb^{III} ions ($4f^{13}$, $J=7/2$, $S=1/2$, $L=3$, $g=8/7$; $^2F_{7/2}$). In complex **1**, upon cooling, the $\chi_M T$ product steadily increases up to 40 K to reach a value of 60.04 $cm^3\,K\,mol^{-1}$ and this is followed by a gradual decrease to reach a value of 21.31 $cm^3\,K\,mol^{-1}$ at 2 K (in presence of 1 T applied magnetic field). The gradual increase of $\chi_M T$ up to 40 K is a clear signature of the presence of weak ferromagnetic interactions in the system (Figure 5 a). The decrease in $\chi_M T$ upon further cooling can be attributed to the combined effects from

Table 2. Structural and magnetic features of tetranuclear lanthanide assemblies having butterfly-shaped core topology.

Compound	Dy_3–(μ_3-OH) distances [Å]	Coordination numbers (local geometries around Ln^{III} centers)	Magnetic properties	Ref.
$[Dy_4(\mu_3\text{-}OH)_2\text{-}(hmmpH)_2(hmmp)_2(Cl)]$ $hmmpH_2 = C_{10}H_{13}NO_3$	2.344, 2.347, and 2.381	eight coordinate (distorted square-antiprism)	SMM $U_{eff} = 7$ K $\tau_0 = 3.8 \times 10^{-5}$ s	[14a]
$[Dy_4(\mu_3\text{-}OH)_2(\mu\text{-}OH)_2(2,2\text{-}bpt)_4(NO_3)_4(EtOH)_2]$ 2,2-bptH $= C_{12}H_9N_5$	2.333, 2.405 and 2.408	eight coordinate (distorted square-antiprism)	SMM $U_{eff} = 80$ K $\tau_0 = 5.75 \times 10^{-6}$ s	[14b]
$[Dy_4(\mu_3\text{-}OH)_2(o\text{-}van)_4(O_2CC(CH_3)_3)_4(NO_3)_2]$ *o*-van $= C_8H_8O_3$	2.337, 2.367 and 2.402	eight coordinate (distorted square antiprismatic geometry)	SMM $U_{eff} = 6.25$ K $\tau_0 = 3.75 \times 10^{-5}$	[14c]
$[Dy_4(\mu_3\text{-}OH)_2(mdeaH)_2(piv)_8]$ $mdeaH_2 = C_5H_{13}NO_2$	2.373, 2.334 and 2.447	eight coordinate (between dodecahedral and bicapped trigonal-prismatic; distorted dodecahedral)	SMM $U_{eff} = 6.2$ $\tau_0 = 2.4 \times 10^{-5}$	[14d]
$[Dy_4(\mu_3\text{-}OH)_2(ampdH_4)_2(piv)_{10}]$ $ampdH_4 = C_6H_{15}NO_2$	2.359, 2.354 and 2.411	eight coordinate (distorted square antiprismatic and distorted bicaped trigonal prismatic)	SMM $U_{eff} = 5.4$ K $\tau_0 = 1.1 \times 10^{-5}$ s	[14e]
$[Dy_4(\mu_3\text{-}OH)_2(bmh)_2(msh)_4Cl_2]$ $bmh = C_{16}H_{16}N_2O_4$ $msh = C_8H_{10}N_2O_2$	2.362, 2.302, and 2.447	seven and eight coordinate	$U_{eff} = 9.7$ K; 170 K $\tau_0 = 3.2 \times 10^{-5}$ s; 4 X10^{-7} s	[14f]
$[Dy_4(\mu_3\text{-}OH)_2L_2(acac)_6]$ $H_2L = C_{20}H_{22}N_2O_2$ $acac = C_5H_8O_2$	2.342, 2.340 and 2.378	eight coordinate (distorted square-antiprism)	$U_{eff} = 22$ K $\tau_0 = 3.66 \times 10^{-6}$ s	[14g]
$[Dy_4(\mu_3\text{-}OH)_2(php)_2(OAc)_6(H_2O)_2]$ $H_2php = C_{19}H_{15}N_7O_2$	2.343, 2.320 and 2.469	eight and ten coordinate	slow relaxation of magnetization	[14h]
$[Dy_4(LH)_2(\mu_3\text{-}OH)_2(\eta^2\text{-}piv)_2(\mu_2\text{-}\ \eta^1{:}\eta^1Piv)_2]$ $LH_4 = C_{19}H_{24}N_4O_5$	2.338, 2.351 and 2.458	eight coordinate (distorted triangular dodecahedral)	$U_{eff =}$ 49.03 K $\tau_{0 =}5.78 \times 10^{-8}$	this work

thermal depopulation of excited state $\pm m_j$ Stark levels of Dy^{III} ions and intra/intermolecular exchange interactions between the Dy^{III} ions.[14c,37m] Contrary to this observed variation, in complex **2** (Figure 5c) the $\chi_M T$ product gradually decreases up to 45 K and then drops rapidly to reach a value of 18.31 $cm^3 K mol^{-1}$ at 2 K (at 0.1 T). For complex **3** (Figure 5e) also the $\chi_M T$ product gradually decreases up to 50 K and then drops rapidly to reach a value of 16.94 $cm^3 K mol^{-1}$ at 2 K (at 1 T). In complex **5**, (Figure 6c) the $\chi_M T$ product decreases rapidly starting from the room temperature to reach a value of 5.12 $cm^3 K mol^{-1}$ at 2 K (at 1 T). This behavior in complexes **2**, **3**, and **5** can be ascribed to the progressive depopulation of excited state $\pm m_j$ stark levels of Tb^{III}, Er^{III}, and Yb^{III} ions, respectively, arising from the $^7F_6$, $^4I_{15/2}$, $^2F_{7/2}$ ground terms, respectively, by the existent antiferromagnetic interactions between the lanthanide ions. For complex **4**, (Figure 6a) the $\chi_M T$ product remains almost constant till 20 K and then finally drops off abruptly to reach values of 20.03 $cm^3 K mol^{-1}$ (at 1 T). This is mainly due to the depopulation of the crystal field $\pm m_j$ states and also possible weak intermolecular interactions between the Ho^{III} ions, which could be responsible for the sharp decreases in $\chi_M T$ at low temperatures. Comparative analysis on all the complexes suggests that, for complex **5**, $\chi_M T$ starts to decline at a higher temperature and this is essentially due to the larger splitting of $^2F_{7/2}$ ground multiplet and preponderant depopulation of the excited state $\pm m_j$ stark levels.

Isothermal magnetization measurements were performed on the polycrystalline samples of **1**–**5**. The field dependence of the magnetization for **1**–**5** at 2, 4, and 6 K (sometimes 8 K) shows a relatively rapid increase in the magnetization to reach almost saturation for magnetic fields larger than 2 T (Figures 5 and 6). Notably, the field dependence of magnetization up to 6 K (some cases 8 K) does not get saturated even at 7 T. This is necessarily due to inherent large magneto-anisotropy of the Ln^{III} ions along with weak intramolecular interactions inducing accessibility of low-lying excited states even at 2 K. In **1**–**5**, the field dependence of magnetization reaches a maximum value of about 21.5, 17.7, 17.8, 20.8, and 7.6 $N\mu_B$, respectively, which are approximately half of the expected values for four weakly coupled lanthanide ions, and can be attributed to the crystal-field effects leading to significant magnetic anisotropy.

Dynamics of magnetization in 1 and 2

In order to probe the dynamics of magnetization, alternating-current (ac) magnetic susceptibility measurements were carried out on complex **1** at 0 and 0.15 T dc field in the temperature range of 2–20 K. At both 0 and 0.15 T magnetic fields, complex **1** displays variable-frequency temperature dependence of the in-phase (χ') and out-of-phase (χ'') susceptibility signals with maxima at 10 and 7.5 K, respectively, at the highest employed frequency of 4111 Hz. Clear, temperature-dependent maxima in the χ' and χ'' signals were observed at and below 10 K. This clearly affirms the presence of SMM behavior. The ac measurements in the presence of static dc field were undertaken in order to suppress the QTM efficiently. Observation of single-peak relaxation behavior is notable as generally Ln^{III} complexes show multiple relaxation phenomena owing to substantial quantum tunneling of magnetization (QTM) at zero field and the presence of crystallographically independent lanthanide

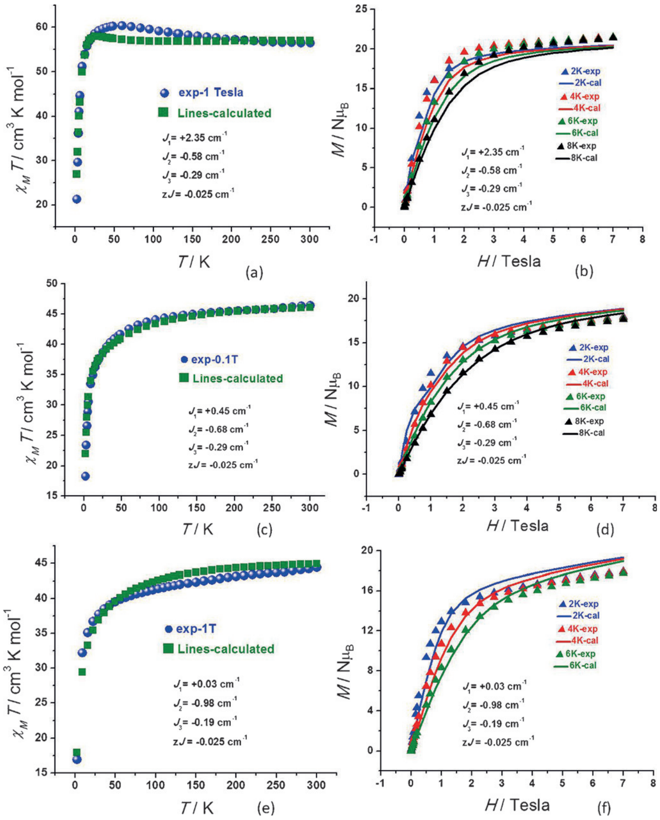

Figure 5. Temperature-dependent $\chi_M T$ plot for complexes a) **1**, c) **2**, and e) **3**; blue-filled circles represent experimental data and green-filled squares correspond to ab initio simulations using three different exchange interactions and constant intermolecular interaction (zJ) of -0.025 cm^{-1}. Field dependence of molar magnetization plots for complexes b) **1**, d) **2**, and f) **3**; filled triangles imply experimental data and solid lines correlate to ab initio simulations using three different exchange interactions and constant intermolecular interaction (zJ) of -0.025 cm^{-1}. It is worth noting that all the J values provided in the graphs correspond to J^{exch} contribution of the total magnetic interaction.

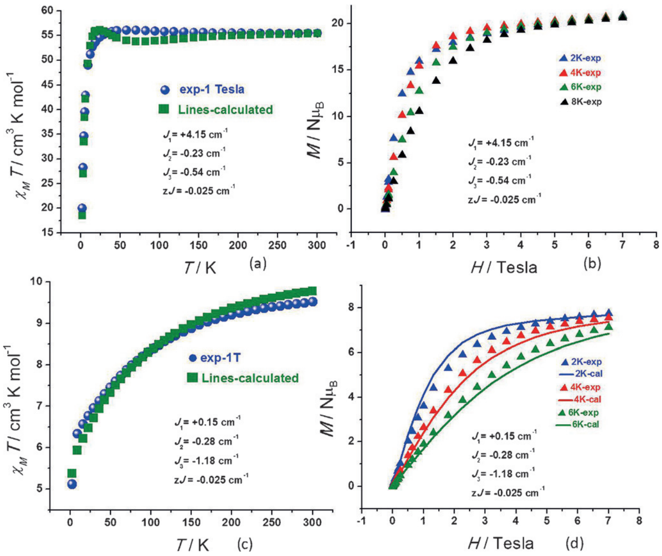

Figure 6. Temperature-dependent $\chi_M T$ plot for complexes a) **4** and c) **5**; blue-filled circles represent experimental data and green-filled squares correspond to ab initio simulations using three different exchange interactions and constant intermolecular interaction (zJ) of -0.025 cm^{-1}. Field dependence of molar magnetization plot for complexes b) **4** and d) **5**; filled triangles imply experimental data and solid lines correlate to ab initio simulations using three different exchange interactions and constant intermolecular interaction (zJ) of -0.025 cm^{-1}. It is worth noting that all the J values provided in the graphs correspond to J^{exch} contribution of the total magnetic interaction. [Note: In complex **5**, the ab initio simulated data could not produce a nice fit with respect to the experimental data.]

sites. The maximum peaks corresponding to χ''/χ' (0/0.15 T) do not go to zero below the maxima at low temperature, suggesting the existence of fast QTM, transverse anisotropy, and hyperfine and dipolar interactions. Detailed analysis of the χ''/χ' versus T plots indicates that for χ' dependence of temperature, relaxation becomes temperature-independent at higher temperature (quantum regime), while the thermally activated relaxation process prevails at lower temperature. On the other hand, for χ'' dependence of temperature is dictated by thermal processes throughout the temperature-variation regime. In temperature-dependent relaxation plots, below the maximum peak, a drop of χ''/χ' is detected with a slight increase of ac response for few frequencies. This increase is attributed to superparamagnetism in conjunction with paramagnetism and prevalent QTM, transverse anisotropy, and hyperfine and dipolar interactions. Besides, alternating-current (ac) magnetic susceptibility measurements were carried out on complex **1** at 0.15 T dc field in the frequency range of 0–4000 Hz. Though variable-temperature frequency dependence behavior of in-phase component of ac susceptibility was visible (below 20 K), no clear signature of maxima could be detected. The out-of-phase ac susceptibility shows a more pronounced frequency dependence (below 20 K; 2–20 K range), but in this case also a maxima could not be detected accurately (except that at low temperatures that is, ca. 5 K a clear maxima was observed). Upon cooling, χ'' shows a maximum and starts to reduce in the 4–8 K range. The characteristic frequency (maximum of χ'' vs. υ plot) at about 5 K for **1** progressively decreases with an increasing dc magnetic field (Figure 7 f). This is suggestive of an operative thermal relaxation mechanism.[29] Hence, analysis of the relaxation dynamics clearly reveals that, despite the inherent fast QTM of lanthanide complexes, the thermally assisted Orbach process seems to be the prevalent relaxation process at low temperature in complex **1**. We have also undertaken ac measurements on complex **2** at 0 and 0.15 T dc field in the temperature range of 2–20 K. In the variable-frequency temperature-dependence plots, no temperature-dependent χ' signal was detected in 0 and 0.15 T of magnetic field (Figure S6 in the Supporting Information). However, a very weak temperature-dependent χ'' signal was observed in the 0 and 0.15 T magnetic fields. In contrast, in the absence of frequency dependent χ'/χ'' signal both at 0 and 0.15 T field suggests the absence of SMM behavior of complex **2** (Figure S6 in the Supporting Information). Moreover, the divergence of χ'' peaks at low temperatures ($<$4 K) in **2** indicates the presence of a fast relaxation process within the ground doublet precluding SMM characteristics in **2**.

The frequency dependence of χ'' has been fitted to a generalized Debye model to extract the relaxation time τ. The fitting of τ to the Arrhenius law leads to the deduction of an effective

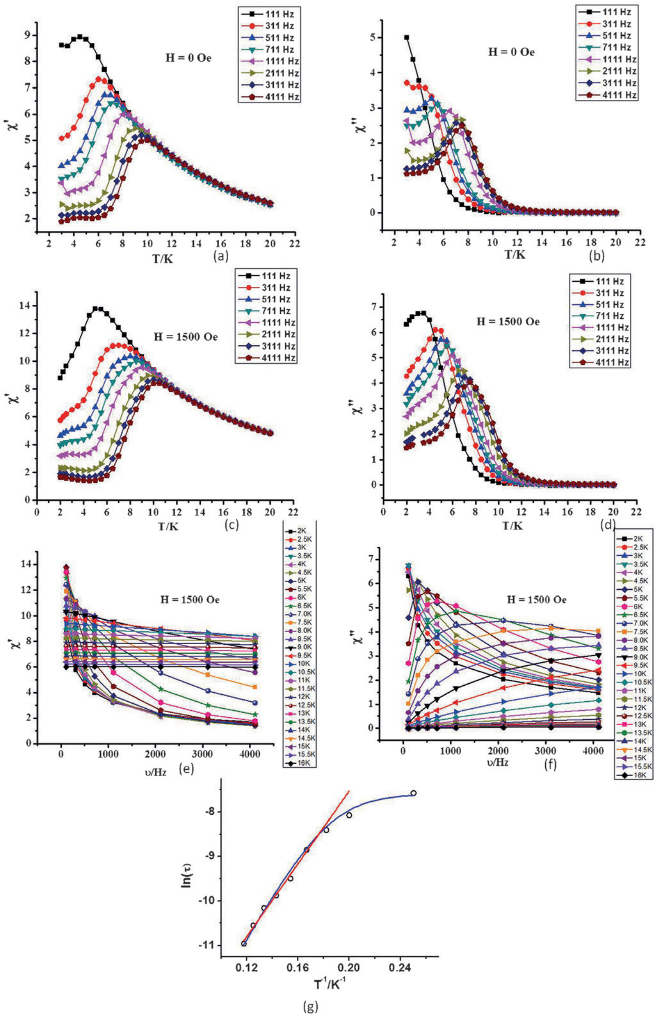

Figure 7. Temperature dependence of the a) in-phase and b) out-of-phase ac susceptibility at 0 T dc applied magnetic field for complex **1**. Temperature dependence of the c) in-phase and d) out-of-phase ac susceptibility at 0.15 T dc applied magnetic field for complex **1**. Frequency dependence of the e) in-phase and f) out-of-phase ac susceptibility at 0.15 T dc applied magnetic field for complex **1** [Note: all the real/imaginary component of magnetic susceptibilities (χ'/χ'') have unit of $cm^3 mol^{-1}$]. g) Arrhenius plots for the relaxation times (τ) extracted from the χ'' versus frequency data in zero Oe dc fields for compound **1**. The solid blue line corresponds to the best fits to QTM plus Orbach (black void circles). The solid red line represents linear fitting of the high-temperature data which consequently signifies Orbach relaxation process.

energy barrier for magnetization reorientation (U_{eff}). The linear dependence of ln(τ) at high temperatures suggests a predominant Orbach relaxation mechanism. The data deviate from linearity in the low-temperature region due to operative QTM and confirms consideration of other spin-lattice relaxation mechanism processes. These relaxation times can be fitted with the Equation (1),[26] and accounts for relaxation through quantum tunneling and Orbach thermal processes.

$$\tau^{-1} = \tau_{QTM}{}^{-1} + \tau_0{}^{-1}\exp(-U_{eff}/k_B T) \qquad (1)$$

This resulted in larger U_{eff} values and smaller flipping rates as compared to the simple Arrhenius law. In Equation (1), $\tau_{QTM}{}^{-1}$ represents the relaxation frequency of the quantum tunneling relaxation process. The fit of the data leads to an effective energy barrier for magnetization reorientation U_{eff} = 49.03 K (34.08 cm^{-1}) with $\tau_0 = 5.78\times10^{-8}$ s and $\tau_{QTM} = 4.13\times10^{-4}$ s for complex **1** (Orbach + QTM). Moreover, fitting of the high-temperature relaxation times to the Arrhenius law (linear Orbach process) results in U_{eff} = 40.92 K (28.44 cm^{-1}) with $\tau_0 = 1.5\times10^{-7}$ s. This again reiterates the prevalence of Orbach mechanism in regulating the relaxation even in the low-temperature region.

Ab initio calculations

To gain insights into the nature of the local anisotropy of the Ln^{III} centers and to understand their electronic structural properties, ab initio calculations were performed on all five complexes. For each complex, we have undertaken two sets of calculations: primarily, using the SINGLE_ANISO program, we have calculated the single-ion magnetic anisotropy of the individual Ln^{III} ions; later, the POLY_ANISO program was employed to extract the exchange-coupled energy levels and the exchange parameters.

Single-ion analysis on complexes 1–5

*Complex **1***: The energy data for eight Kramers doublets (KDs) of the ground $^6H_{15/2}$ multiplet for the four Dy^{III} ions and g tensors of ground state in compound **1** are shown in the Supporting Information, with the excited states lying at 3000 cm^{-1}. In **1**, the ground state KD shows an almost axial type anisotropy for all the four metal sites (see Table S5 in the Supporting Information); that is, g_z (Figure 8, yellow dashed lines for orientation of main anisotropy axis for ground KDs in all the four Dy^{III} sites) is close to that expected for a pure $m_J = \pm15/2$ state. It is worthwhile mentioning that all the computed g tensors correspond to an effective spin $\tilde{s} = 1/2$ of the KDs. Besides, in all the Dy sites, the angle between g_z directions of ground and first excited KD lies in the range of about 30–50°. This invoked relaxation to be operative by means of first excited KDs in all four metal centers. Based on single-ion analysis, the calculation energy barrier (U_{calcd}) for magnetization reorientation turns out to be 146 and 118 cm^{-1} for two types of non-equivalent Dy^{III} centers (Dy1, Dy3 and Dy2, Dy4, respectively). Crystal field analysis shows predominant non-axial terms and axial contributions reiterating considerable competitiveness between them (see Table S6 in the Supporting Information). This corresponds to the significant ground KD QTM and affirms the SMM characteristic only in the presence of an applied dc magnetic field in **1**.

Comparatively larger values of g_z and negligible magnitude of transverse anisotropy clearly reveals axial nature of the ground KD of each KD involved in exchange interaction. This axial nature essentially ensures interaction between the neighboring Dy^{III} ions to be of Ising type.

*Complex **2***: The energy data for the thirteen energy levels of the ground $^7F_6$ multiplet for the four Tb^{III} ions and g tensors of ground state in compound **2** are shown in the Supporting In-

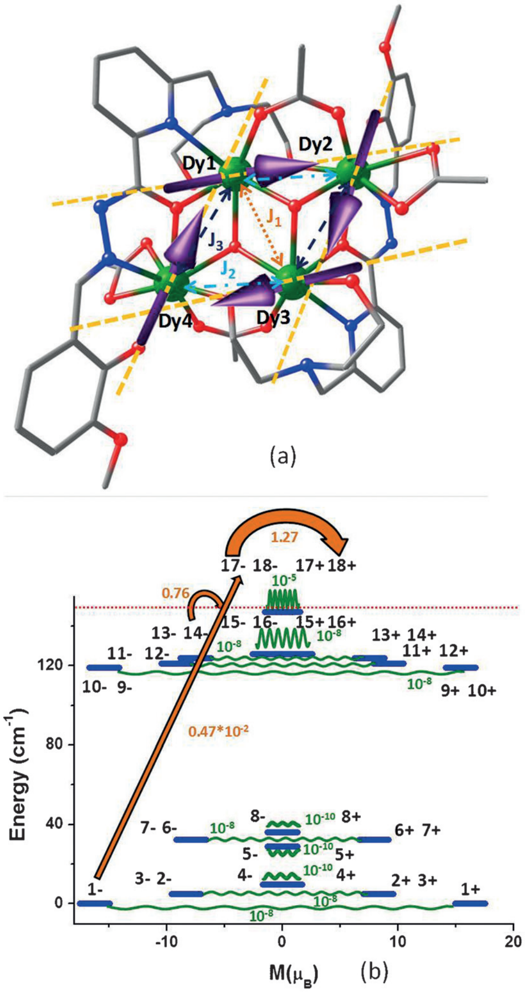

Figure 8. a) Crystal structure of complex **1** showing main anisotropy axis (yellow dashed lines) on four Dy^{III} ions and local magnetization (purple arrows) in the ground state. The diagram also illustrates exchange pathways employed for our calculations. b) Low-lying exchange spectrum and the position of the magnetization blocking barrier (red dotted line) in complex **1**. Every exchange state (represented by thick blue lines) has been arranged based on the corresponding magnetic moment. The curved green arrows signify tunneling transition ($\Delta_{tun;}$ tunnel splitting or tunnel gaps) within each doublet, orange bent arrows indicate spin-phonon transitions (numbers are averaged transition moments in μ_B connecting the corresponding states). It is worth noting that the spin-phonon transition among the lowest energy states are not mentioned as they lie in the range of about 10^{-1} to 10^{-4} μ_B.

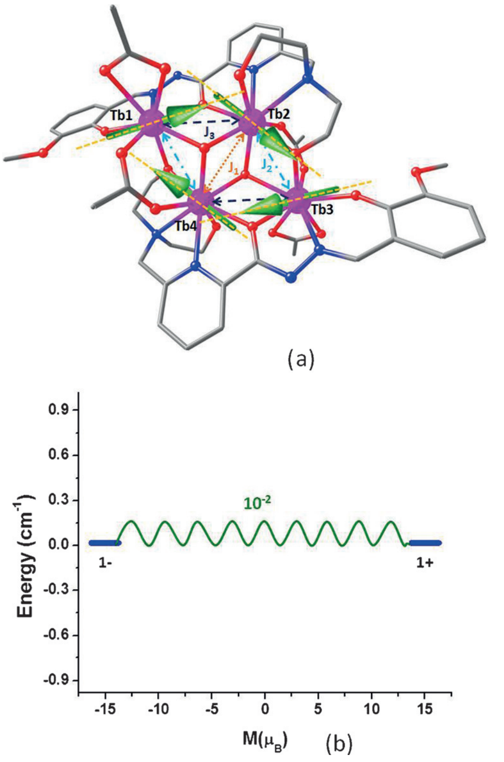

Figure 9. a) Crystal structure of complex **2** showing main anisotropy axis (yellow dashed lines) on four Tb^{III} ions and local magnetization (light green arrows) in the ground state. The diagram also illustrates exchange pathways employed for our calculations. b) Low-lying exchange spectrum in complex **2**. Every exchange state (represented by thick blue lines) has been arranged based on the corresponding magnetic moment. The curved green arrows signify tunneling transition ($\Delta_{tun;}$ tunnel splitting or tunnel gaps) within each doublet.

formation (see Table S7), with the excited states lying at 2200 cm^{-1}. In **2**, the ground as well as excited state pseudo-doublets show an Ising type anisotropy (due to completely zero g_{xy} contribution in non-Kramers ions in accordance with Griffith Theorem) for all four metal sites, that is, g_z (Figure 9, yellow dashed lines for orientation of main anisotropy axis for ground pseudo-doublet in all the four Tb^{III} sites) is close to that expected for a pure $m_j = \pm 6$ state. Based on single-ion analysis, significant Δ_{tun} was computed within the ground pseudo-doublets as 5 and 1 cm^{-1} for two types of non-equivalent Tb^{III} centers (Tb1,Tb3 and Tb2,Tb4, respectively) . This is evidence for substantial ground multiplet crystal field perturbation and precludes any SMM behaviour in complex **2**. Crystal field analysis shows the competitive nature of significant axial and non-axial terms (see Table S8). This corroborates the earlier observed large tunnel splitting and is responsible for the lack of SMM characteristics in complex **2**.

Complex **3**: The energy data for eight KDs of the ground $^4I_{15/2}$ multiplet for the four Er^{III} ions and g tensors of ground state in compound **3** are shown in the Supporting Information (see Table S9), with the excited states lying at 6600 cm^{-1}. In **3**, the ground state KD possesses significant transverse anisotropy for all four metal sites promoting QTM probability within the ground KD ($g_z = 16$, $g_x = 0.3$, $g_y = 0.7$; see Figure 10: yellow dashed lines represent orientation of main anisotropy axis for ground KD in all the four Er^{III} sites). Besides, in all the Er sites, the angle between g_z directions of ground and first excited KD lies in the range of about 65–132°. This invoked relaxation to be operative through the first excited KD in all the four metal centers. Based on single-ion analysis, substantial QTM relaxation pathway completely removes the possession of SMM characteristics in complex **3**. Based on crystal field analysis, non-axial contributions prevail (see Table S10) and this precludes SMM behavior in complex **3**.

Complex **4**: The energy spectrum for seventeen energy levels of the ground $^5I_8$ multiplet for the four Ho^{III} ions and g tensors of ground state in compound **4** are shown in the Sup-

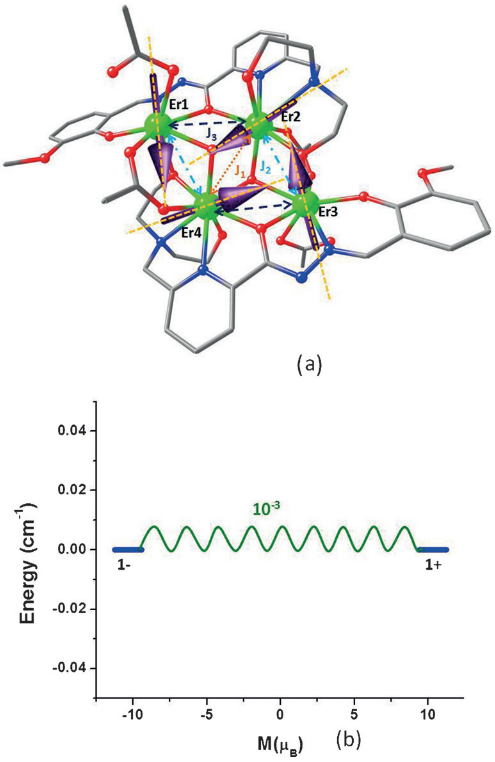

Figure 10. a) Crystal structure of complex **3** showing main anisotropy axis (yellow dashed lines) on four Er^{III} ions and local magnetization (purple arrows) in the ground state. The diagram also illustrates exchange pathways employed for our calculations. b) Low-lying exchange spectrum in complex **3**. Every exchange state (represented by thick blue lines) has been arranged based on the corresponding magnetic moment. The curved green arrows signify tunneling transition ($\Delta_{tun;}$ tunnel splitting or tunnel gaps) within each doublet.

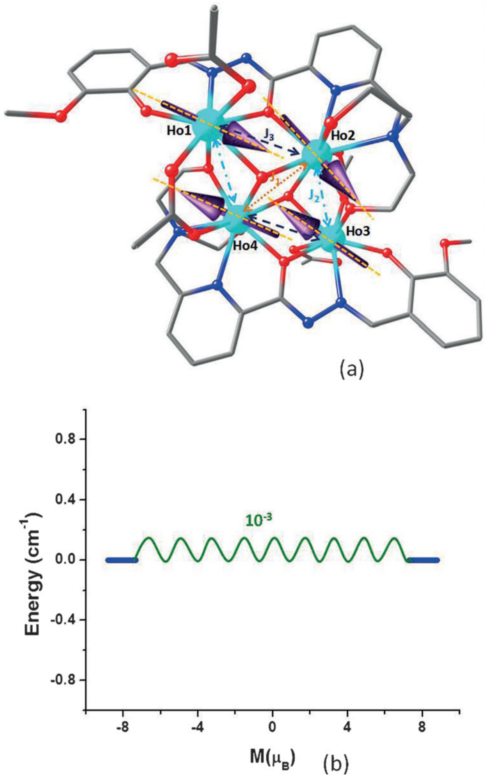

Figure 11. a) Crystal structure of complex **4** showing main anisotropy axis (yellow dashed lines) on four Ho^{III} ions and local magnetization (purple arrows) in the ground state. The diagram also illustrates exchange pathways employed for our calculations. b) Low-lying exchange spectrum in complex **4**. Every exchange state (represented by thick blue lines) has been arranged based on the corresponding magnetic moment. The curved green arrows signify tunneling transition ($\Delta_{tun;}$ tunnel splitting or tunnel gaps) within each doublet.

porting Information (see Table S11), with the excited states lying at 5200 cm^{-1}. In **4**, the ground as well as excited state pseudo-doublets show an pure Ising type anisotropy for all four metal sites; that is, g_z (see Figure 11: yellow dashed lines represent orientation of main anisotropy axis for ground pseudo-doublet in all the four Ho^{III} sites) is close to that expected for a pure $m_j = \pm 8$ state. Based on single-ion analysis, significant Δ_{tun} was computed within the ground pseudo-doublets as 1.1 and 0.7 cm^{-1} for two types of non-equivalent Ho^{III} centers (Ho1,Ho3 and Ho2,Ho4) respectively. This precludes any SMM behaviour in complex **4**. Crystal field analysis (see Table S12) shows preponderant non-axial terms and leads to the absence of SMM behaviour in complex **4**.

*Complex **5**:* The energy spectrum for eight KDs of the ground $^2F_{7/2}$ multiplet for the four Yb^{III} ions and *g* tensors of ground state in compound **5** are shown in the Supporting Information (see Table S13), with the excited states lying at 10 000 cm^{-1}. In **5**, the ground state KD transverse component prevails with $g_x = 5.23$, $g_y = 3.34$, $g_z = 0.92$ for all the metal centers. This clearly corresponds to the stabilization of $m_j = \pm 1/2$ state and occurrence of pronounced QTM relaxation pathway (Figure 12 a yellow dashed lines for orientation of main anisotropy axis for ground KD in all the four Yb^{III} sites). This solely blocks the magnetization within ground state KD and forces relaxation within ground state itself, deterring attainment of any energy barrier for magnetization reversal. Based on single-ion analysis, substantial QTM relaxation pathway completely removes the possession of SMM characteristics in complex **5**. Crystal field analysis (see Table S14) shows significantly larger non-axial terms and leads to the absence of SMM behavior in complex **5**.

Exchange interaction and SMT behavior analysis on complexes 1–5

Due to the Ising nature of the Dy^{III} sites, we have simulated the magnetic interactions between Dy^{III} ions by incorporating contributions from magnetic dipole–dipole and exchange interactions within an Ising exchange Hamiltonian. We have computed the exchange interaction between the Dy^{III} ions within the Lines[38] model, with an effective Heisenberg Hamiltonian [Eq. (2)],[17b,c] (in which $J_i = J_i^{dipolar} + J_i^{exch}$; that is, J_i is the total magnetic interaction in combination of calculated $J_i^{dipolar}$ and fitted J_i^{exch} parameters; this summation depicts the interaction between all the neighboring Dy^{III} centers) corresponding to local $S = 5/2$ spins on Dy^{III} centers in the absence of spin-

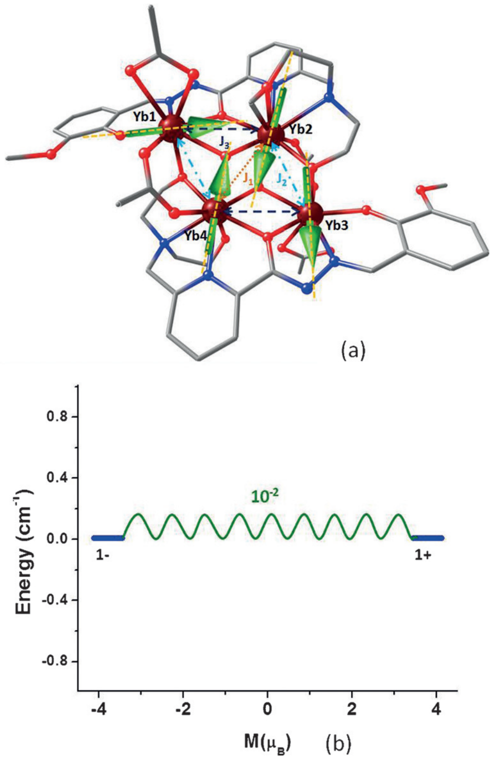

Figure 12. a) Crystal structure of complex **5** showing main anisotropy axis (yellow dashed lines) on four Yb^{III} ions and local magnetization (light green arrows) in the ground state. The diagram also illustrates exchange pathways employed for our calculations. b) Low-lying exchange spectrum in complex **5**. Every exchange state (represented by thick blue lines) has been arranged based on the corresponding magnetic moment. The curved green arrows signify tunneling transition ($\Delta_{tun;}$ tunnel splitting or tunnel gaps) within each doublet.

orbit coupling which has been diagonalized based on the KDs procured from fragment ab initio calculations.

$$\hat{H}_{ex} = -\sum\nolimits_{i=1}^{3} J_i \cdot S_i \cdot S_{i+1} \tag{2}$$

The fitting was performed with three different exchange interactions J_1–J_3, while the intermolecular interaction (zJ) was kept constant for all complexes. It is worth noting that in the POLY_ANISO code, the dipolar contribution is treated explicitly, while the exchange part has been estimated from fit to the magnetic data. Magnetic coupling between Ln ions incorporate contributions from magnetic dipole–dipole and exchange interactions. This approach proves to be appropriate in this regard due to the resemblance of the KDs to $|M_J = \pm 15/2\rangle$ state. We also calculated the exchange spectrum (Figure 8 b) of complex **1** using the POLY_ANISO program. Nice agreement between the simulated and experimental magnetic data ($\chi_M T$ (T) and M (H)) was (Figure 5 a, b) observed with the parameters $J_1 = +2.35$ cm^{-1}, $J_2 = -0.58$ cm^{-1}, and $J_3 = -0.29$ cm^{-1} at an intermolecular interaction (zJ) $= -0.025$ cm^{-1}.

Considering the small value of exchange, it is expected to be of Ising type [Eq. (3)], in which $\tilde{S}_{iz}$ represents projection of the pseudo-spin on the anisotropy axis of i^{th} center and also depicts two states with reverse maximal magnetization on this center.

$$\tilde{H}_{ex} = -\sum\nolimits_{i=1}^{3} \tilde{J}_i \tilde{S}_{iz} \tilde{S}_{i+1z} \tag{3}$$

Concepts based on the Lines model and Equation (3) has led to the deduction of Equation (4) in which $\phi_{i,j+1}$ corresponds to angle between the anisotropy axes on the centers i and $i+1$.

$$\tilde{J}_i = 25 \cos \phi_{i,j+1} J_i \tag{4}$$

As $\phi_{i,j+1} \approx 2\pi/3$, $\tilde{J}_i = -12.5\ J_i$.[30] For our calculations, we will assume $J_i = J$ ($\tilde{J}_i = \tilde{J}$). Now, based on this approximation, we can state that $\tilde{J}_1$, $\tilde{J}_2$, and $\tilde{J}_3$ will be antiferromagnetic, ferromagnetic, and ferromagnetic, respectively, for ferromagnetic, antiferromagnetic, and antiferromagnetic J_1, J_2, and J_3, respectively This results in ferromagnetic alignment of the pseudospins (as represented by local magnetization vector in Figure 8 a purple arrows) along the anisotropy axis (as represented by yellow dashed line in Figure 8 a). This leads to tangential orientation of local magnetization vectors along the four Dy^{III} centers. Lines model calculations leads to the formation of exchange spectrum of lowest exchange levels. The resultant Ising doublets are represented by one single direction of magnetization Z and this varies in accordance with the doublets as well as zero transversal magnetization ($g_x = g_y = 0$). Our data clearly reveals comparatively stronger dipolar Dy^{III}–Dy^{III} coupling (Table 3) than the corresponding exchange contribution and this is in line with the expected behavior for Dy^{III}–Dy^{III} coupling. Non-compensation of the spins owing to the non-parallel axes leads to a non-zero magnetic ground state ($g_z = 32.42$, $g_z = g_z =$ ca. 10^{-8}; highly anisotropic ground exchange doublet) with the next-higher exchange doublet state lying at 4.86 cm^{-1} above the ground state possessing g_z of 39.61. This results in large ground state magnetic moment as $\mu_z = {}^1\!/_2\, g_z \mu_B$[27] $=$ 16.21 μ_B, that is, almost twice the moment of an individual Dy^{III} center. It is notable that, along with ground state, all the ex-

Table 3. Parameters of the magnetic interaction between the Tb^{III}, Er^{III}, Ho^{III} and Yb^{III} ions in complexes **1–5**.

	J_1	J_2	J_3
complex **1**			
$J_i^{dipolar}$	3.10	−1.30	−1.30
J_i^{exch}	+2.35	−0.58	−0.29
J_i	+5.45	−1.88	−1.59
complex **2**			
$J_i^{dipolar}$	+1.00	−0.40	−0.50
J_i^{exch}	+0.45	−0.68	−0.29
J_i	+1.45	−1.08	−0.79
complex **3**			
$J_i^{dipolar}$	+0.60	−0.50	−0.70
J_i^{exch}	+0.03	−0.98	−0.19
J_i	+0.63	−1.48	−0.89
complex **4**			
$J_i^{dipolar}$	−1.10	−0.90	−1.10
J_i^{exch}	+4.15	−0.23	−0.54
J_i	+3.05	−1.13	−1.64
complex **5**			
$J_i^{dipolar}$	+0.70	−0.40	−0.60
J_i^{exch}	+0.15	−0.28	−1.18
J_i	+0.85	−0.68	−1.78

Table 4. Energies [cm^{-1}], corresponding tunnel splitting (Δ_{tun}) and g_z values of the low-lying exchange doublet state in complex **1**:

Energy	Δ_{tun}	g_z	Energy	Δ_{tun}	g_z
0	10^{-8}	32.42	118.97	10^{-8}	34.05
4.86	10^{-8}	39.61	121.03	10^{-8}	31.47
4.86	10^{-8}	39.59	121.03	10^{-8}	31.48
9.70	10^{-10}	71.90	123.83	10^{-8}	50.79
28.96	10^{-10}	0.05	123.83	10^{-8}	50.79
32.44	10^{-8}	39.26	125.87	10^{-8}	60.74
32.44	10^{-8}	39.26	125.87	10^{-8}	60.74
35.93	10^{-10}	0.02	147.12	10^{-5}	14.76
118.97	10^{-8}	34.09	147.12	10^{-5}	14.78

change excited doublets are associated with substantial magnetic moment (Table 4). Such a low-energy gap between the ground and excited states (4.86 cm^{-1}) in conjunction with large magnetic moment of first excited exchange doublet ($g_z = 39.61$) is probably the reason behind the absence of a prominent S-shape in the low-field *M*(*H*) curve (Figure 5 b). Due to the magnetic exchange, the local magnetization vector and main anisotropy axis are found to be collinear, leading to a non-compensated ground state magnetic moment. Hence, the combination of ferromagnetic orientation of the pseudospins on Dy sites and the significant magnetic moment of Dy sites in the ground exchange doublet leads to the presence of a toroidal magnetic moment in complex **1** and categorizes it under a mixed moment single-molecule toroic (SMT).

The pure Ising nature of the pseudo-doublets for all the four Tb^{III} and Ho^{III} sites in complexes **2** and **4**, respectively, ensures the interaction between the neighboring Tb^{III} and Ho^{III} ions to be of Ising type. However, substantial transverse components in all the eight/four KDs for all the four Er^{III} and Yb^{III} sites in complex **3** and **5**, respectively, prevents the interaction between the neighboring Er^{III} and Yb^{III} ions to be of pure Ising type. In all four complexes, we have simulated the magnetic interactions by incorporating contributions from magnetic dipole–dipole and exchange interactions within an Ising exchange Hamiltonian using the POLY_ANISO program. A nice agreement between the simulated and experimental magnetic data ($\chi_M T(T)$ and *M*(*H*)) was observed (see Figure 5 c, d, e, f and Figure 6 a, b, c, d for complexes **2**, **3**, **4** and **5** respectively) with the parameters $J_1 = +0.45$ cm^{-1}, $J_2 = -0.68$ cm^{-1} and $J_3 = -0.29$ cm^{-1} at intermolecular interaction $(zJ) = -0.025$ cm^{-1} in complex **2**, $J_1 = +0.03$ cm^{-1}, $J_2 = -0.98$ cm^{-1} and $J_3 = -0.19$ cm^{-1} at intermolecular interaction $(zJ) = -0.025$ cm^{-1} in complex **3**, $J_1 = +4.15$ cm^{-1}, $J_2 = -0.23$ cm^{-1} and $J_3 = -0.54$ cm^{-1} at intermolecular interaction $(zJ) = -0.025$ cm^{-1} for complex **4** and $J_1 = +0.15$ cm^{-1}, $J_2 = -0.28$ cm^{-1} and $J_3 = -1.18$ cm^{-1} at intermolecular interaction $(zJ) = -0.025$ cm^{-1} in complex **5** (Table 3). Now, based on this approximation, we can state that.$\tilde{J}_1$, $\tilde{J}_2$, $\tilde{J}_3$ will be antiferromagnetic, ferromagnetic, and ferromagnetic, respectively, for ferromagnetic, antiferromagnetic, and antiferromagnetic J_1, J_2, and J_3, respectively, in all four complexes (**2**–**5**).

The three different exchange interactions result in ferromagnetic alignment of the pseudospins (as represented by local magnetization vector in Figure 9 a purple arrows) along the anisotropy axis (as represented by yellow dashed line in Figure 9 a) in **2**. This leads to tangential orientation of local magnetization vectors along the four Tb^{III} centers forming a parallelogram along the Tb$_4$ plane. Our data clearly reveals comparatively stronger dipolar Tb^{III}–Tb^{III} coupling (see Table 3) than the corresponding exchange contribution. Non-compensation of the spins owing to the non-parallel axes leads to a non-zero magnetic ground state ($g_z = 30.10$, $g_x = g_y =$ ca. 10^{-8}) with the next- higher exchange doublet state lying at 7.29 cm^{-1} above the ground state possessing g_z of 0.34. This results in large ground state magnetic moment as $\mu_z = {}^1\!/_2\, g_z = 15.05\ \mu_B$; that is, almost twice the moment of an individual Tb^{III} center. It is notable that excited exchange doublets higher than the ground state are associated with zero magnetic moment while few of the excited exchange doublets contain large magnetic moment (Table 5). From Figure 9 a, it is evident that the magnetic moments of the four Tb ions are projected onto the Tb$_4$ plane with a toroidal arrangement. Such a low-energy gap between the ground and excited states (7.29 cm^{-1}) in conjunction with a weakly magnetic ($g_z = 0.34$) first excited state explains the absence of prominent S shape in low-field experimental *M*(*H*) curve (Figure 5 d). Due to the magnetic exchange, local magnetization vector and main anisotropy axis are found to be collinear leading to non-compensated ground state magnetic moment. Hence, combination of ferromagnetic orientation of the pseudo-spins on Tb sites and significant magnetic moment of Tb sites in ground exchange doublet leads to the presence of toroidal magnetic moment in complex **2** and categorizes it under a mixed-moment single-molecule toroic (SMT).

Table 5. Energies [cm^{-1}], corresponding tunnel splitting (Δ_{tun}) and g_z values of the low-lying exchange doublet state in complexes **2**–**5**.

Energy	Δ_{tun}	g_z	Energy	Δ_{tun}	g_z
complex **2**					
0	0.05	30.10	8.34	0.10	0.06
7.29	0.002	0.34	14.42	0.006	26.50
7.97	0.08	0.06	14.56	0.10	23.92
complex **3**					
0	0.001	20.67	2.04	0.001	21.46
0.48	0.004	18.97	2.24	0.001	22.78
0.64	0.003	16.47	2.63	0.0002	45.85
complex **4**					
0	0.002	16.12	5.42	0.002	73.43
2.70	0.002	11.11	28.05	0.001	0.13
2.74	0.003	11.09	30.99	0.002	37.80
complex **5**					
0	0.02	7.59	0.40	0.03	5.31
0.22	0. 02	3.65	0.43	0.03	6.68
0.32	0.06	6.81	0.47	0.04	5.47

The three exchange interactions in complex **3**, **4**, and **5** result in ferromagnetic alignment of the pseudospins (Figures 10 a, 11 a and 12 a for **3**, **4**, and **5**, respectively, as indicated by purple and light green arrows respectively; see, also Table 3) along the anisotropy axis (as represented by yellow dashed line in Figures 10 a, 11 a and 12 a for **3**, **4**, and **5**, respectively).

Despite this ferromagnetic orientation, the corresponding magnetic moments do not form a wheel-shaped topology, which is a signature for toroidal behavior. Instead they lie in very random fashion and preclude possession of any toroidal magnetic moment in the complexes **3**–**5**.

Non-compensation of the spins owing to the non-coparallel axes leads to a non-zero magnetic ground state $g_z = 30.10$, $g_x = g_y =$ ca. 10^{-7} in **3**, $g_z = 16.12$, $g_x = g_y =$ ca. 10^{-8} in **4** and $g_z = 7.59$, $g_x = g_y =$ ca. 10^{-8} in **5** (see Table 5). In all the three complexes, the next-higher exchange doublet state lies at 0.48, 2.70, and 0.22 cm^{-1} with respect to the ground state possessing g_z of 18.97, 11.11, and 3.65 for **3**, **4**, and **5**, respectively. This results in a large ground state magnetic moment of $\mu_z = \frac{1}{2} g_z = 10.34$, 8.06, and 3.79 μ_B for **3**, **4**, and **5**, respectively (see Table 5). In all the three complexes, the magnetic moment for the exchange coupled system is almost equal to the magnetic moment of an individual Er^{III}, Ho^{III}, and Yb^{III} center.

Analyzing the mechanism of magnetization relaxation in complexes 1–5

To gain further insights into the relaxation pathways operative in complex **1**, we need to analyze the exchange spectrum (Figure 8 b). The tunnel splitting of the ground state is very small till the sixteenth exchange doublet ($< 10^{-5}\ \text{cm}^{-1}$) (Figure 8 b, green curved arrows). This suppresses the ground state QTM completely and TA-QTM within the higher excited energy levels up to sixteenth exchange doublet and promotes relaxation through higher levels. The seventeenth and eighteenth exchange doublet possess Δ_{tun} of about $10^{-5}\ \text{cm}^{-1}$ and this unfolds a channel for tunneling relaxation of magnetization through these states. Towards estimating the energy barrier, we need to consider spin–phonon mechanisms (Orbach, Raman) through the excited states. This relies on the largest transition magnetic moments corresponding to the connecting exchange states (orange bent arrows in Figure 8 b). Though significant matrix elements corresponding to a spin–phonon transition have been detected between the ± 14 and ± 15 states (0.76 μ_B), due to concomitant negligible tunnel splitting, relaxation through this pathway can be discarded. On this note, the relaxation path through -17, -18, $+18$, and $+17$ should be efficient, as tunnel splitting between these states is intrinsically large; that is, at the cut-off range of $10^{-5}\ \text{cm}^{-1}$. In addition, a large magnetic moment matrix element between the -17, $+18$ and -18, $+17$ states (1.27 μ_B) separated by 0.005 cm^{-1} essentially induces the relaxation by this pathway. Moreover, spin-phonon transition from the ground state -1 to -18 and -1 to $+18$ is associated with magnetic moment matrix element of about 10^{-2} and 10^{-1} μ_B, respectively. This relaxation mechanism outlines the computed energy barrier for magnetization reorientation approximately as about 147 cm^{-1} in complex **1**. The intra-square exchange coupling within the four Dy^{III} centers has been well represented by the exchange energy[29c] spectrum in Figure 13. The U_{calcd} value estimated is larger than that obtained from the experiments (U_{eff}) and the discrepancy could be attributed to various factors, such as intermolecular interactions and non-Orbach multi-phonon relaxation processes, which are known to play a proactive role in the relaxation of magnetization.[37h,j,39]

To gain further insights into the relaxation pathways operative in complex **2** we need to analyze the exchange spectrum (Figure 9 b). The tunnel splitting within the ground state itself is very large ($10^{-2}\ \text{cm}^{-1}$) (Figure 9 b, green curved arrows). This promotes QTM/TA-QTM efficiently and precludes any SMM behavior. Hence, though complex **1** shows both SMM and SMT behavior, complex **2** only shows SMT characteristics (the lack of SMM behavior is due to large tunneling transition within the ground exchange doublet).

In a similar manner, with an aim to analyze relaxation pathways operative in complexes **3**, **4**, **5** we need to analyze the exchange spectrum (see Figure 10 b, Figure 11 b and Figure 12 b). The tunnel splitting within the ground state itself is very large: 10^{-3}, 10^{-3}, $10^{-2}\ \text{cm}^{-1}$ for complexes **3**, **4**, and **5**, respectively (Figures 10 b, 11 b, and 12 b green curved arrows for **3**, **4**, and **5**, respectively). This promotes QTM/TA-QTM efficiently and precludes any SMM behavior. Hence, complex **3**, **4**, and **5** lack both SMM and SMT characteristics.

Comparative studies on complexes 1–5

The pre-requisite for SMT behavior is strong uniaxial anisotropy in a low-symmetry ligand field environment.[15a] Additionally, large intramolecular dipolar coupling induced by the local magnetic moments on the interacting magnetic centers contributes to the observation of SMT characteristics.[15a] As per these two criteria, Dy^{III} has the largest anisotropy due to an intrinsically large angular momentum and spin-orbit coupling. Among the complexes studied, **1** possesses the strongest intramolecular dipolar coupling ($J_1 = +3.10\ \text{cm}^{-1}$, $J_2 = -1.30\ \text{cm}^{-1}$, $J_3 = -1.30\ \text{cm}^{-1}$; see Table 3). These factors cumulatively are responsible for the observation of toroidal moment in the ground state in **1**. On the other hand, in the rest of the four complexes, intramolecular J_{dipolar} is weaker than in **1** lying in the range of about -1 to $+1\ \text{cm}^{-1}$. Despite possessing second strongest dipolar exchange (after Dy), complex **4** lacks SMT characteristic. However, with relatively weaker dipolar coupling ($J_1 = +1.00\ \text{cm}^{-1}$, $J_2 = -0.40\ \text{cm}^{-1}$, $J_3 = -0.50\ \text{cm}^{-1}$; see Table 3), complex **2** is predicted to exhibit mixed moment SMT behavior. This is due to incumbent vortex-type wheel-shaped arrangement between the local magnetic moments on the four interacting Tb^{III} sites in **2**. On the other hand, local magnetic moments on the four interacting Ho^{III} centers are oriented in a random fashion and prevent SMT behavior in **4** and this may be attributed to the decrease in the oblate nature as we move from Dy^{III} to Ho^{III} ions.[1c] This consequentially leads to a reduction in the overall negative charged axial crystal field around Ho, deterring perfect perpendicular orientation of g_z with respect to the oblate electron density. Except complex **1**, none of other complexes exhibit SMM behavior. This is also associated with the presence of strong exchange interactions in complex **1** which suppress the QTM to promote relaxation via higher energy levels. Absence of SMM behavior in complex **4**, despite the presence of strong exchange, is due to very weak

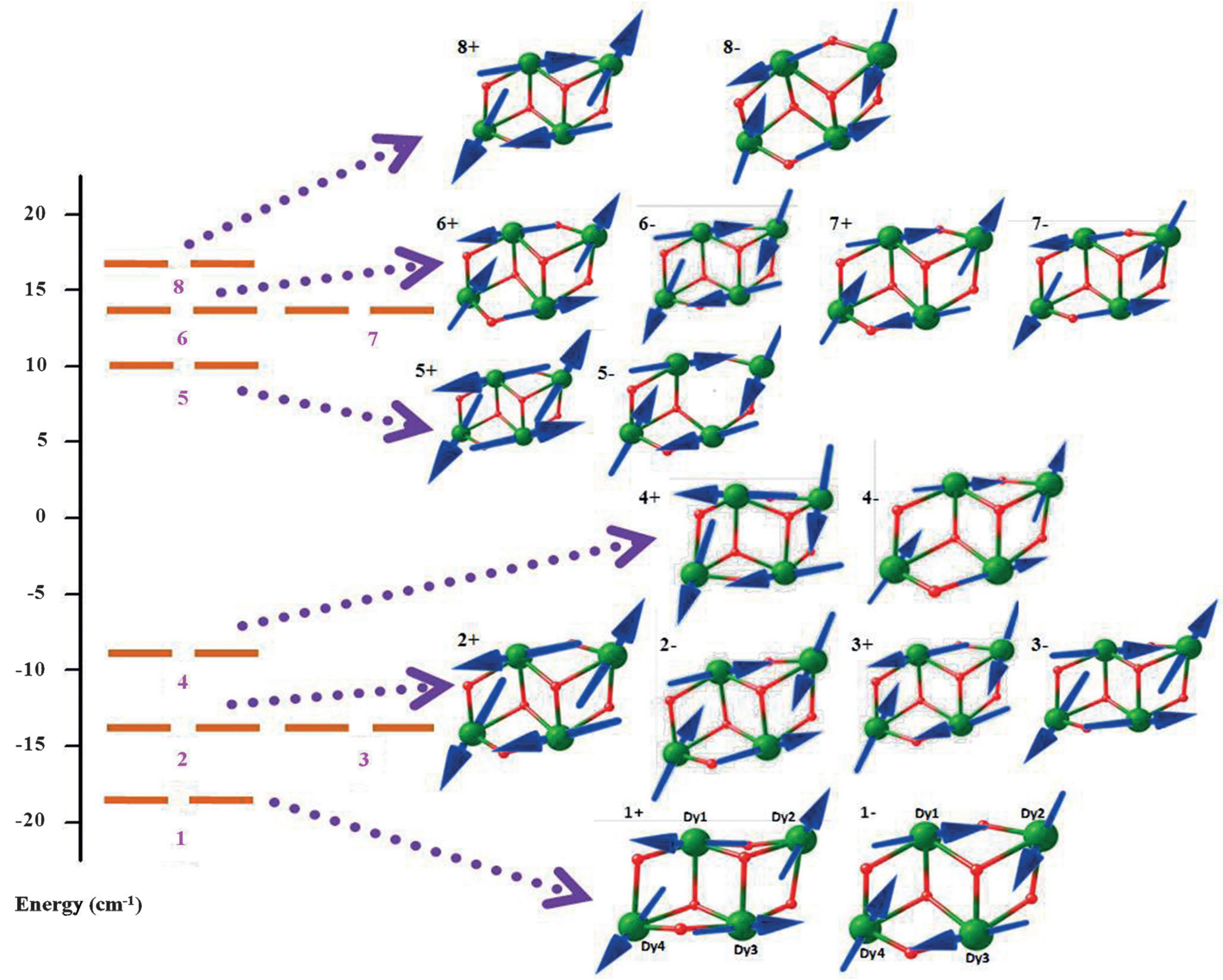

Figure 13. Computed exchange energy spectrum for complex **1** where energies are expressed in cm^{-1}. The orange lines for each degenerate energy level correspond to the number of degenerate states associated to that level. The tetranuclear core Dy_4 structural motifs have been used to represent the local magnetic moments of the Ising quantum states. The eigenstates are correlated to each other by flips of magnetic moments (blue arrows) on the four individual Dy^{III} magnetic centers. The pink numbers indicate number of the exchange doublet. For each exchange doublet two time reversed components possessing + and − opposite magnetization exist and are shown in the above picture.

exchange promoted among these ions, leading to prominent QTM effects at the ground state.

Conclusions

In summary, we have synthesized a series of homometallic tetranuclear complexes by employing a new aroylhydrazone based Schiff base ligand. These complexes possess a butterfly-shaped structural topology. Ab initio calculations were carried out on these isostructural Ln^{III}_4 ($Ln = Dy^{III}$, Tb^{III}, Er^{III}, Ho^{III}, and Yb^{III}) complexes with an aim to understand the anisotropy orientation, exchange coupled spectra, and toroidal magnetic moments. Complex **1** shows both SMM and SMT (mixed moment) behavior with a calculated barrier of $119\,cm^{-1}$. Complex **2** shows SMT behavior, but SMM characteristics could not be detected. Our comparative analysis reveals that complexes **3**, **4** and **5**, with total magnetic moments equal to that of their intrinsic metal centers, lack SMT behavior. This can be attributed to the inability of accurate communication between the magnetic moments of the neighboring magnetic sites to induce SMT characteristic. In addition, absence of SMM in **3**, **4**, and **5** is suggestive of prevalent single-ion behavior over exchange interaction. Strong exchange interaction is expected to quench the QTM probability to promote relaxation via higher excited states.

Experimental Section

Solvents and other general reagents used in this work were purified according to standard procedures.[31] Pyridine-2,6-dicarboxylic acid, sodium borohydride, $Dy(NO_3)_3{\cdot}5\,H_2O$, $Tb(NO_3)_3{\cdot}5\,H_2O$, $Ho(NO_3)_3{\cdot}5\,H_2O$, $Er(NO_3)_3{\cdot}5\,H_2O$ and $Yb(NO_3)_3{\cdot}5\,H_2O$ were obtained from Sigma Aldrich Chemical Co. and were used as received. *o*-Vanillin, hydrazine hydrate (80%), PBr_3, pivalic acid, diethanolamine and sodium sulphate (anhydrous) were obtained from S.D. Fine Chemicals, Mumbai (India). Methyl-6-(hydroxymethyl) picolinate[27a] and methyl 6-(bromomethyl)picolinate, were prepared according to literature procedures.[27a]

Instrumentation: Melting points were measured using a JSGW melting point apparatus and are uncorrected. IR spectra were recorded as KBr pellets on a Bruker Vector 22 FT IR spectrophotometer operating at 400–4000 cm^{-1}. Elemental analyses of the compounds were obtained from Thermoquest CE instruments CHNS-O, EA/110 model. ^1H NMR spectra were recorded in $CDCl_3$ and CD_3OD on a JEOL JNM LAMBDA 400 model spectrometer operating at 500·0 MHz, Chemical shifts are reported in parts per million (ppm) and are referenced with respect to internal tetramethylsilane (^1H).

X-ray crystallography: The crystal data for the compounds have been collected on a Bruker SMART CCD diffractometer (MoKα radiation, $\lambda = 0.71073$ Å). The program SMART[32a] was used for collecting frames of data, indexing reflections, and determining lattice parameters, SAINT[32a] for integration of the intensity of reflections and scaling, SADABS[32b] for absorption correction, and SHELXTL[32c,d] for space group and structure determination and least-squares refinements on F^2. All the structures were solved by direct methods using the program SHELXS-97[32e] and refined by full-matrix least-squares methods against F^2 with SHELXL-97.[32e] Hydrogen atoms were fixed at calculated positions and their positions were refined by a riding model. All the non-hydrogen atoms were refined with anisotropic displacement parameters. All the structures encounter thermal disorder for few atoms, especially in the tertiary butyl groups of the main residues. Hence we had to employ some restrains/constrains for the refinement stability. In complex **2**, the carbon atom of the –OMe and interstitial $CHCl_3$ were showing large thermal displacements. Hence, electron densities of corresponding atoms were partitioned into two positions and refined with suitable constraints. The crystallographic figures have been generated using Diamond 3.1e software.[32f] The crystal data and the cell parameters for compounds **1**–**3** are summarized in Table 6. CCDC 1490848 (**1**), 1490849 (**2**), 1490850 (**3**), 1490851 (**4**), and 1490852 (**5**) contain the supplementary crystallographic data for this paper. These data can be obtained free of charge from The Cambridge Crystallographic Data Centre.

Magnetic measurements: Magnetic data were measured using a Quantum Design MPMS-XL SQUID magnetometer. All samples were 3 mm diameter pellets molded from ground crystalline samples. Magnetic susceptibility measurements were carried out in the 2–300 K temperature range in a 0.1 or 1 T applied magnetic field, and diamagnetic corrections were considered by Pascal's constants. Isothermal magnetization measurements were undertaken up to 7 T at 2, 4, 6 and in somecases 8 K. The ac susceptibility measurements under different applied static fields were performed using an oscillating ac field of 3.5 Oe and ac frequencies ranging from 10 to 10 000 Hz.

Computational details: The magnetic properties of all the Ln^{III} sites in complexes **1**–**5** were studied by fragment ab initio calculations. In order to have good illustration of the 3d or 4f ligand field states within a fragment we needed to consider the impact of neighboring metal centers. Owing to the concomitant limitations of MOLCAS (8.0 version)[25a–e] of computing magnetic properties of single paramagnetic metal ion at a time, we undertook calculations on individual metal fragments. In all the complexes, four types of calculations were carried out. For each fragmented calculation, one Ln^{III} ion of interest was kept intact, while the other three atoms were replaced by the diamagnetic Y^{III} ion. All the calculations were carried out on X-ray crystal structures using the basis sets[33] shown in Table 7, embedded in MOLCAS suite:

In each fragment calculation, multi-configurational approach relativistic effects were treated in two steps based on a Douglas–Kroll Hamiltonian. For the generation of basis sets, scalar terms were in-

Table 6. Crystal data and structure refinement parameters of **1**–**5**.

	1	**2**	**3**	**4**	**5**
formula	$C_{60}H_{92}Dy_4N_8O_{24}$	$C_{64}H_{86}Cl_{18}N_8O_{20}Tb_4$	$C_{60}H_{92}Er_4N_8O_{24}$	$C_{60}H_{92}Ho_4N_8O_{24}$	$C_{60}H_{90}N_8O_{24}Yb_4$
M_w [g^{-1}]	1959.42	2561.23	1978.46	1969.14	1999.56
crystal system	monoclinic	monoclinic	monoclinic	monoclinic	monoclinic
space group	$P2_1/n$	$P2_1/c$	$P2_1/n$	$P2_1/n$	$P2_1/n$
a [Å]	12.661(6)	11.484(3)	12.634(3)	12.642(5)	12.635(5
b [Å]	16.590 (7)	20.047(5)	16.602(4)	16.632(5)	16.646(5)
c [Å]	16.934(7)	20.750(5)	16.906(4)	16.943(5)	16.848(5)
β [°]	94.421(1)	103.869 (3)	94.630(4)	94.424(5)	94.612(5)
V [$Å^{-3}$]	3546.5(3)	4638(2)	3534.5(15)	3552(2)	3532(2)
Z	2	2	2	2	2
ρ_{calcd} [$g\,cm^{-3}$]	1.835	1.834	1.859	1.841	1.880
μ [mm^{-1}]	4.246	3.596	4.781	4.487	5.327
$F(000)$	1928.0	2504.0	1944.0	1936.0	1956.0
crystal size [mm^3]	0.0046×0.0031×0.0025	0.059×0.052×0.037	0.0082×0.0056×0.0049	0.0096×0.0091×0.0065	0.059×0.052×0.037
θ range [°]	4.08 to 25.03	4.09 to 25.03	4.09 to 25.03	4.08 to 25.03	4.10 to 25.03
limiting indices	$-15 \leq h \leq 15$ $-19 \leq k \leq 19$ $-20 \leq l \leq 20$	$-13 \leq h \leq 13$ $-18 \leq k \leq 23$ $-24 \leq l \leq 24$	$-15 \leq h \leq 14$ $-19 \leq k \leq 19$ $-17 \leq l \leq 20$	$-10 \leq h \leq 15$ $-19 \leq k \leq 19$ $-20 \leq l \leq 20$	$-14 \leq h \leq 15$ $-19 \leq k \leq 9$ $-20 \leq l \leq 18$
reflns collected	19 795	28 257	22 329	23 853	17 858
independent reflns	6227 [R(int) = 0.0357]	8121 [R(int) = 0.0682]	6205 [R(int) = 0.0477]	6236 [R(int) = 0.0281]	6171 [R(int) = 0.0386]
completeness to θ [%]	99.5	99.2	99.5	99.5	99.2
data/restraints/parameters	6227/4/458	8121/9/474	6205/4/439	6236/2/440	6171/1/377
goodness-of-fit on F^2	1.027	1.044	1.019	1.079	1.077
final R indices [$I > 2\theta(I)$]	$R_1 = 0.0252$ $wR_2 = 0.0483$	$R_1 = 0.0540$ $wR_2 = 0.1410$	$R_1 = 0.0258$ $wR_2 = 0.0530$	$R_1 = 0.0187$ $wR_2 = 0.0448$	$R_1 = 0.0347$ $wR_2 = 0.0822$
R indices (all data)	$R_1 = 0.0370$ $wR_2 = 0.0510$	$R_1 = 0.0676$ $wR_2 = 0.1520$	$R_1 = 0.0359$ $wR_2 = 0.0561$	$R_1 = 0.0205$ $wR_2 = 0.0455$	$R_1 = 0.0441$ $wR_2 = 0.0964$

Table 7.

Elements	Basis set	Elements	Basis set
Dy	ANO-RCC..8s7p5d3f2g1h.	Y	ANO-RCC..6s5p3d.
Tb	ANO-RCC..8s7p5d3f2g1h.	N	ANO-RCC..3s2p1d.
Er	ANO-RCC..8s7p5d3f2g1h.	O	ANO-RCC..3s2p1d.
Ho	ANO-RCC..8s7p5d3f2g1h.	C	ANO-RCC..3s2p.
Yb	ANO-RCC..8s7p5d3f2g1h.	H	ANO-RCC..2s.

cluded that were used to determine spin-free wave functions and energies through the use of complete active space self-consistent field (CASSCF)[34] methods. Spin-orbit coupling was taken into account by using RASSI-SO,[35] which uses CASSCF wave functions as the basis sets and multi-configurational wave functions as input states. The resulting wave functions and the energies of the molecular multiplets were used for the evaluation of the magnetic properties, and *g* tensors of the lowest multiplets of the isolated fragments were calculated using a specially designed routine SINGLE_ANISO.[25f] The basis of this approach is essentially ab initio calculation of all orbital moment and magnetic moment matrix elements on the relevant spin-orbit multiplets acquired from CASSCF/RASSI-SO calculations. These matrix elements were subsequently utilized in SINGLE_ANISO routine to compute:

1) experimentally measured magnetic proprties (temperature-dependent Van Vleck susceptibility tensor, field-dependent magnetization for different temperatures and temperature-dependent magnetization at various frequencies)

2) parameters of magnetic spin Hamiltonians for different spin-orbit multiplets, spin states represented by the corresponding pseudospin (*g* tensors).

For the estimation of magnetic properties, all spin-orbit multiplets of crystal field on the Ln^{III} centers were considered. This feature was imperative for precise quantitative depiction of the impact of strong magnetic anisotropy and applied magnetic field.

Upon describing the individual metal ion properties, we attempted to elucidate the exchange coupling between the Ln^{III} centers within the Lines model as implemented in the POLY_ANISO[26] routine and validated earlier.[14c,15,18a,34,36,37] This uses a single-parameter exchange Hamiltonian to explain the isotropic interaction between spin terms in absence of spin-orbit coupling. Spin-orbit multiplets on monometallic fragments were generated usually in terms of Heisenberg Hamiltonian. Diagonalization of this matrix led to the evaluation of anisotropic interaction between the respective metal centers. It is notable that the Lines model[38,15–17] employs only single parameter for the effective isotropic interaction in order to simulate the anisotropic interaction between metal pair fragments. This allowed the use of specific different exchange parameters corresponding to the accurate description of respective spin terms of the metal fragments. The Lines model considers three cases : 1) two strong anisotropic centers (Ising exchange), 2) two isotropic (spin-only) magnetic sites (Heisenberg exchange/Ising exchange), and 3) one isotropic and one strong anisotropic center (Ising+Heisenberg). In the POLY_ANISO code, we used the Ising exchange Hamiltonian (as equation mentioned in main manuscript) in which the Lines model precisely incorporates anisotropic dipolar and exchange interactions.

Synthesis

Methyl 6-{[bis(2-hydroxyethyl)amino]methyl}picolinate: To a solution of diethanolamine (0.956 g, 9.1 mmol) in THF (40 mL), under constant stirring, triethylamine (3.62 mL, 27.3 mmol) was added added dropwise and the reaction mixture was allowed to stir for 20 min at room temperature. Then, methyl 6-(bromomethyl)picolinate (2.1 g, 9.1 mmol) in THF was added dropwise over a period of 15 min. The reaction mixture was stirred for 24 h at room temperature. The white turbid solution was filtered and evaporated in vacuo to get a light yellow oily residue, which was dissolved in dichloromethane (30 mL) and washed with water (30 mL) and brine (20 mL). The aqueous layer was extracted twice with dichloromethane (2×30 mL) and the combined organic layer was dried (Na_2SO_4) and filtered, and the solvent was removed in vacuo affording a light yellow oily product. Yield: 1.95 g, 83.51%; ^1H NMR (500 MHz, $CDCl_3$): $\delta = 2.84$ (t, 4H; NCH_2), 3.57 (t, 4H; CH_2O), 3.94 (s, 3H; OMe), 3.97 (s, 2H; NCH_2), 5.28 (s, 1H; OH), 7.43 (d, 1H; Py-H), 7.79 (t, 1H; Py-H), 8.01 ppm (d, 1H; Py-H); elemental analysis calcd for $C_{12}H_{18}N_2O_4$ (254.28): C 56.68, H 7.13, N 11.02; found: C 56.62, H 7.01, N 11.15.

Methyl 6-{[bis(2-hydroxyethyl)amino]methyl}picolinohydrazide: A solution of methyl 6-[{bis(2-hydroxyethyl)amino}methyl]picolinate (1.8 g, 7.08 mmol) in ethanol (15 mL) was added dropwise to a stirred solution of hydrazine hydrate (0.425 g, 8.5 mmol) at room temperature and the resulting solution was heated to reflux for 5 h. After allowing the reaction mixture to come to room temperature, ethanol was removed off in vacuo to produce a light yellow solid residue, which was recrystallized from MeOH/$CHCl_3$ (1:1) to get the final product as a light yellow solid. Yield: 1.6 g, 88.92%; m.p. 97 °C; ^1H NMR (500 MHz, CD_3OD): $\delta = 2.72$ (t, 4H; NCH_2), 3.62 (t, 4H; CH_2O), 3.90 (s, 2H; NCH_2), 7.64 (d, 2H; Py-H), 7.89 ppm (t, 1H; Py-H); elemental analysis calcd for $C_{11}H_{18}N_4O_3$ (254.13): C 51.96, H 7.13, N 22.03; found: C 52.02, H 7.50, N 22.11.

6-{[Bis(2-hydroxyethyl)amino]methyl}-*N'*-(2-hydroxy-3-methoxybenzylidene)picolinohydrazide (LH_4): To a stirred solution of methyl 6-{[bis(2-hydroxyethyl)amino]methyl}picolinohydrazide (1.5 g, 5.9 mmol) in methanol (40 mL), *o*-vanilin (0.898 g, 5.9 mmol) in methanol (20 mL) was added dropwise at room temperature, and the resulting solution was heated to reflux for 5 h. After allowing the reaction mixture to come to room temperature, the yellow solution was concentrated in vacuo and kept in a refrigerator overnight. An off-white precipitate was filtered, washed with cold methanol (30 mL) and diethyl ether (20 mL) before being dried to get the title product. Yield: 1.63 g, 71.11%; m.p. 104 °C; ^1H NMR (500 MHz, $CDCl_3$): $\delta = 2.86$ (t, 4H; NCH_2), 3.71 (t, 4H; CH_2O), 3.92 (s, 3H; OMe), 4.00 (s, 2H; NCH_2), 6.83 (t, 1H; Ar-H), 6.92 (d, 1H; Ar-H), 7.16 (d, 1H; Ar-H), 7.25 (d, 1H; Py-H), 7.61 (t, 1H; Py-H), 8.04 (d, 2H; Py-H), 8.39 (s, 1H; imine-H), 11.32 (br, 1H; NH), 11.78 ppm (s, 1H; OH); FT-IR (KBr): $\tilde{\nu} = 3438$ (O–H), 3231 (N–H); 1682 (C=O), 1607 ($C{=}N_{imine}$), 1594 cm^{-1} ($C{=}N_{py}$); ESI-MS: *m/z*: $[M+H]^+$: 389.17; elemental analysis calcd for $C_{19}H_{24}N_4O_5$ (388.42): C 58.75, H 6.23, N 14.42; found: C 58.96, H 6.03, N 14.97.

General synthetic procedure for the preparation of the complexes 1–5: All the metal complexes (**1–5**) were synthesized according to the following procedure. To a stirred solution of LH_4 (0.046 g, 0.12 mmol) in methanol (20 mL), $Ln(NO_3)_3{\cdot}5H_2O$ (0.24 mmol) was added affording a yellow solution, which was stirred for a further period of 10 min. After that, triethylamine (0.09 mL, 0.6 mmol) was added dropwise to the mixture at room temperature and the reaction mixture was continued to stir for a further period of 15 min. At this stage pivalic acid (0.025 g, 0.24 mmol) was added dropwise and the stirring was continued for 12 h to get a yellow precipitate. This was filtered, washed with diethyl ether (2×20 mL), dried, re-dissolved in (1:1) v/v mixture of methanol and chloroform and kept for crystallization. Within a week, yellow block-shaped crystals, suitable for X-ray crystallography study, were obtained by slow evaporation the solvents. The details of each reaction and characterization data for these complexes (**1**–**5**) are given below.

$[Dy_4(LH)_2(\mu_2\text{-}\eta^1\eta^1Piv)_2(\eta^2\text{-}Piv)_2(\mu_3\text{-}OH)_2]\cdot 2\,H_2O\cdot 2\,MeOH$ (1): Quantities: LH_4 (0.046 g, 0.12 mmol), $Dy(NO_3)_3\cdot 5\,H_2O$ (0.107 g, 0.24 mmol), Et_3N (0.09 mL, 0.6 mmol), PivH (0.025 g, 0.24 mmol). Yield: 0.069 g, 59.48% (based on the ligand); m.p. $>250\,^{\circ}C$ (decomp); IR (KBr): $\tilde{\nu}=3645$ (w), 3532 (b), 3051 (b), 2957 (s), 2908 (b), 2863 (w), 1610 (s), 1557 (s), 1480 (s), 1446 (s), 1423 (s), 1375 (s), 1360 (s), 1349 (s), 1237 (s), 1213 (s), 1181 (w), 1167 (w), 1132 (w), 1081 (s), 1034 (w), 1017 (w), 974 (w), 951 (s), 908 (w), 892 (s), 862 (w), 850 (s), 791 (s), 760 (w), 732 (w), 691 (w), 598 (w), 569 (w), 537 (w), 487 cm^{-1} (w); elemental analysis calcd for $C_{60}H_{92}Dy_4N_8O_{24}$ (1959.42): C 36.78, H 4.73, N 5.72; found: C 36.97, H 4.51, N 5.13.

$[Tb_4(LH)_2(\mu_2\text{-}\eta^1\eta^1Piv)_2(\eta^2\text{-}Piv)_2(\mu_3\text{-}OH)_2]\cdot 6\,CHCl_3$ (2): Quantities: LH_4 (0.046 g, 0.12 mmol), $Tb(NO_3)_3\cdot 5\,H_2O$ (0.104 g, 0.24 mmol), Et_3N (0.09 mL, 0.6 mmol), PivH (0.025 g, 0.24 mmol); Yield: 0.068 g, 45.03% (based on ligand); m.p. $>250\,^{\circ}C$ (decomp). IR (KBr): $\tilde{\nu}=$ 3641 (w), 3534 (b), 3041 (b), 2953 (s), 2901 (b), 2865 (w), 1602 (s), 1553 (s), 1486 (s), 1449(s), 1419 (s), 1376 (s), 1363 (s), 1342 (s), 1241 (s), 1209 (s), 1179 (w), 1161 (w), 1128 (w), 1077 (s), 1035 (w), 1015 (w), 971 (w), 946 (s), 903(w), 889 (s), 865 (w), 843 (s), 794 (s), 765 (w), 734 (w), 686 (w), 597 (w), 559 (w), 534(w), 481 cm^{-1} (w); elemental analysis calcd for $C_{64}H_{86}Cl_{18}N_8O_{20}Tb_4$ (2561.23): C 30.01, H 3.38, N 4.38; found: C 30.67, H 3.49, N 4.63.

$[Er_4(LH)_2(\mu_2\text{-}\eta^1\eta^1Piv)_2(\eta^2\text{-}Piv)_2(\mu_3\text{-}OH)_2]\cdot 2\,H_2O\cdot 2\,MeOH$ (3): Quantities: LH_4 (0.046 g, 0.12 mmol), $Er(NO_3)_3\cdot 5\,H_2O$ (0.106 g, 0.24 mmol), Et_3N (0.09 mL, 0.6 mmol), PivH (0.025 g, 0.24 mmol); Yield: 0.065 g, 54.16% (based on ligand); m.p. $>250\,^{\circ}C$ (decomp); IR (KBr): $\tilde{\nu}=$ 3645 (w), 3531 (b), 3039 (b), 2957 (s), 2897 (b), 2861 (w), 1604 (s), 1557 (s), 1481 (s), 1444(s), 1415 (s), 1379 (s), 1361 (s), 1346 (s), 1237 (s), 1201 (s), 1173 (w), 1156 (w), 1122 (w), 1073 (s), 1034 (w), 1012 (w), 978 (w), 946 (s), 902(w), 887 (s), 869 (w), 841 (s), 799 (s), 763 (w), 738 (w), 687 (w), 593 (w), 552 (w), 531(w), 477 cm^{-1} (w); elemental analysis calcd for $C_{60}H_{92}Er_4N_8O_{24}$ (1978.46): C 36.43, H 4.69, N 5.66; found: C 36.75, H 4.33, N 5.79.

$[HO_4(LH)_2(\mu_2\text{-}\eta^1\eta^1PIV)_2(\eta^2\text{-}PIV)_2(\mu_3\text{-}OH)_2]\cdot 2\,H_2O\cdot 2\,MeOH$ (4): Quantities: LH_4 (0.046 g, 0.12 mmol), $Ho(NO_3)_3\cdot 5\,H_2O$ (0.105 g, 0.24 mmol), Et_3N (0.09 mL, 0.6 mmol), PivH (0.025 g, 0.24 mmol); Yield: 0.071 g, 61.2% (based on ligand); m.p. $>250\,^{\circ}C$ (decomp); IR (KBr): $\tilde{\nu}=$ 3639 (w), 3537 (b), 3033 (b), 2955 (s), 2891 (b), 2859 (w), 1602 (s), 1559 (s), 1473 (s), 1447(s), 1410 (s), 1373 (s), 1364 (s), 1343 (s), 1232 (s), 1205 (s), 1177 (w), 1153 (w), 1121 (w), 1068 (s), 1031 (w), 1014 (w), 973 (w), 947 (s), 908(w), 889 (s), 863 (w), 847 (s), 799 (s), 765 (w), 731 (w), 683 (w), 591 (w), 558 (w), 526(w), 472 cm^{-1} (w); elemental analysis calcd for $C_{60}H_{92}Ho_4N_8O_{24}$ (1969.14): C 36.60, H 4.71, N 5.69; found: C 36.94, H 4.79, N 6.01.

$[Yb_4(LH)_2(\mu_2\text{-}\eta^1\eta^1Piv)_2(\eta^2\text{-}Piv)_2(\mu_3\text{-}OH)_2]\cdot 2\,H_2O\cdot 2\,MeOH$ (5): Quantities: LH_4 (0.046 g, 0.12 mmol), $Yb(NO_3)_3\cdot 5\,H_2O$ (0.105 g, 0.24 mmol), Et_3N (0.09 mL, 0.6 mmol), PivH (0.025 g, 0.24 mmol); Yield: 0.063 g, 53.38% (based on ligand); m.p. $>250\,^{\circ}C$ (decomp); IR (KBr): $\tilde{\nu}=$ 3634 (w), 3531 (b), 3037 (b), 2956 (s), 2892 (b), 2853 (w), 1599 (s), 1558 (s), 1471 (s), 1443(s), 1407 (s), 1374 (s), 1368 (s), 1341(s), 1237 (s), 1201 (s), 1173 (w), 1157 (w), 1119 (w), 1061 (s), 1026 (w), 1012 (w), 977 (w), 942 (s), 903(w), 882 (s), 867 (w), 841 (s), 798 (s), 763 (w), 725 (w), 681 (w), 594 (w), 553 (w), 521(w), 468 cm^{-1} (w); elemental analysis calcd for $C_{60}H_{90}N_8O_{24}Yb_4$ (1999.56): C 36.04, H 4.54, N 5.60; found: C 36.34, H 4.12, N 5.89.

Acknowledgements

We thank the Department of Science and Technology (DST), India, for financial support, including support for a single-crystal CCD X-ray diffractometer facility at IIT-Kanpur. V.C. is grateful to the DST for a J. C. Bose Fellowship. S.B. thanks the Council of Scientific and Industrial Research, India, for Senior Research Fellowship. G.R. acknowledges IITB for the High Performance Computing Facility.

Keywords: cluster compounds · lanthanides · magnetic properties · Schiff base · single-molecule magnets

[1] a) R. A. Layfield, *Organometallics* **2014**, *33*, 1084 – 1099; b) J. Luzona, R. Sessoli, *Dalton Trans.* **2012**, *41*, 13556 – 13567; c) J. D. Rinehart, J. R. Long, *Chem. Sci.* **2011**, *2*, 2078 – 2085; d) D. N. Woodruff, R. E. P. Winpenny, R. A. Layfield, *Chem. Rev.* **2013**, *113*, 5110 – 5148; e) S. Y. Lin, J. Tang, *Polyhedron* **2014**, *83*, 185 – 196.

[2] a) R. Sessoli, D. Gatteschi, A. Caneschi, M. A. Novak, *Nature* **1993**, *365*, 141 – 143; b) R. Sessoli, L. Hui, A. R. Schake, S. Wang, J. B. Vincent, K. Folting, D. Gatteschi, G. Christou, *J. Am. Chem. Soc.* **1993**, *115*, 1804 – 1816.

[3] a) J. Long, R. Vallat, R. A. S. Ferreira, L. D. Carlos, F. A. Almeida Paz, Y. Guari, J. Larionova, *Chem. Commun.* **2012**, *48*, 9974 – 9976; b) M. Menelaou, F. Ouharrou, L. Rodríguez, O. Roubeau, S. J. Teat, N. Aliaga-Alcalde, *Chem. Eur. J.* **2012**, *18*, 11545 – 11549; c) M. Jeletic, P. H. Lin, J. J. Le Roy, I. Korobkov, S. I. Gorelsky, M. Murugesu, *J. Am. Chem. Soc.* **2011**, *133*, 19286 – 19289; d) S. D. Jiang, B. W. Wang, G. Su, Z. M. Wang, S. Gao, *Angew. Chem. Int. Ed.* **2010**, *49*, 7448 – 7451; *Angew. Chem.* **2010**, *122*, 7610 – 7613; e) S. Cardona-Serra, J. M. Clemente-Juan, E. Coronado, A. Gaita-Arino, A. Camon, M. Evangelisti, F. Luis, M. J. Martinez-Perez, J. Sese, *J. Am. Chem. Soc.* **2012**, *134*, 14982 – 14990; f) R. A. A. Cassaro, S. G. Reis, T. S. Araujo, P. Lahti, M. Miguel, A. Novak, M. G. F. Vaz, *Inorg. Chem.* **2015**, *54*, 9381 – 9383; g) L. Chatelain, F. Tuna, J. Pecautab, M. Mazzanti, *Chem. Commun.* **2015**, *51*, 11309 – 11312.

[4] a) J. L. Liu, K. Yuan, J. D. Leng, L. Ungur, W. Wernsdorfer, F. S. Guo, L. F. Chibotaru, M. L. Tong, *Inorg. Chem.* **2012**, *51*, 8538 – 8544; b) S. D. Jiang, B. W. Wang, H. L. Sun, Z. M. Wan, S. Gao, *J. Am. Chem. Soc.* **2011**, *133*, 4730 – 4733; c) A. K. Bar, C. Pichona, J. P. Sutter, *Coord. Chem. Rev.* **2016**, *308*, 346 – 380; d) M. Yadav, V. Mereacre, S. Lebedkin, M. M. Kappes, A. K. Powell, P. W. Roesky, *Inorg. Chem.* **2015**, *54*, 773 – 781; e) Y. C. Chen, J. L. Liu, L. Ungur, J. Liu, Q. W. Li, L. F. Wang, Z. Ping, L. F. Chibotaru, X. M. Chen, M. L. Tong, *J. Am. Chem. Soc.* **2016**, *138*, 2829 – 2837; f) J. Liu, Y. C. Chen, J. L. Liu, V. Vieru, L. Ungur, J. H. Jia, L. F. Chibotaru, Y. Lan, W. Wernsdorfer, S. Gao, X. M. Chen, M. L. Tong, *J. Am. Chem. Soc.* **2016**, *138*, 5441 – 5450.

[5] a) V. Chandrasekhar, A. Dey, A. J. Mota, E. Colacio, *Inorg. Chem.* **2013**, *52*, 4554 – 4561; b) T. Glaser, *Chem. Commun.* **2011**, *47*, 116 – 130; c) D. W. Boukhvalov, V. V. Dobrovitski, P. Kögerler, M. Al-Saqer, M. Katsnelson, A. I. Lichtenstein, B. N. Harmon, *Inorg. Chem.* **2010**, *49*, 10902 – 10906; d) R. Inglis, L. F. Jones, G. Karotsis, A. Collins, S. Parsons, S. P. Perlepes, W. Wernsdorfer, K. E. Brechin, *Chem. Commun.* **2008**, 5924 – 5926; e) D. E. Bürgler, V. He, T. Esat, S. Fahrendorf, F. Matthes, C. M. Schneider, C. Besson, P. Kögerler, A. Ghi, *Surf. Sci. Nanotech.* **2016**, *14*, 17 – 22; f) F. Shao, B. Cahier, N. Guihery, E. Riviere, A. L. Barra, Y. Lan, W. Wernsdorfer, V. E. Campbell, T. Mallah, *Chem. Commun.* **2015**, *51*, 16475 – 16478; g) R. Sato, K. Suzuki, T. Minato, M. Shinoe, K. Yamaguchi, N. Mizuno, *Chem. Commun.* **2015**, *51*, 4081 – 4084; h) A. K. Bar, C. Pichon, N. Gogoi, C. Duhayon, S. Ramaseshac, J. P. Sutter, *Chem. Commun.* **2015**, *51*, 3616 – 3619.

[6] a) V. Chandrasekhar, P. Bag, W. Kroener, K. Gieb, P. Müller, *Inorg. Chem.* **2013**, *52*, 13078 – 13086; b) G. P. Guedes, S. Soriano, L. A. Mercante, N. L. Speziali, M. A. Novak, M. Andruh, M. G. F. Vaz, *Inorg. Chem.* **2013**, *52*, 8309 – 8311; c) V. Chandrasekhar, B. M. Pandian, R. Boomishankar, A. Steiner, J. J. Vittal, A. Hour, R. Clérac, *Inorg. Chem.* **2008**, *47*, 4918 – 4929; d) O. Iasco, G. Novitchi, E. Jeanneau, D. Luneau, *Inorg. Chem.* **2013**, *52*, 8723 – 8731; e) V. Chandrasekhar, P. Bag, M. Speldrich, J. V. Leusen, P. Kö-

gerler, *Inorg. Chem.* **2013**, *52*, 5035 – 5044; f) V. Chandrasekhar, S. Das, A. Dey, S. Hossain, S. Kundu, E. Colacio, *Eur. J. Inorg. Chem.* **2014**, 397 – 406; g) S. Hossain, S. Das, A. Chakraborty, F. Lloret, J. C. E. Pardo, V. Chandrasekhar, *Dalton Trans.* **2014**, *43*, 10164 – 10174; h) E. Terazzi, G. Rogez, J. L. Gallani, B. Donnio, *J. Am. Chem. Soc.* **2013**, *135*, 2708 – 2722; i) P. Bag, A. Chakraborty, G. Rogez, V. Chandrasekhar, *Inorg. Chem.* **2014**, *53*, 6524 – 6533; j) I. Oyarzabal, B. Artetxe, A. R. Diéguez, J. Á. García, J. M. Seco, E. Colacio, *Dalton Trans.* **2016**, *45*, 9712 – 9726; k) S. K. Langley, C. Le, L. Ungur, B. Moubaraki, B. F. Abrahams, L. F. Chibotaru, K. S. Murray, *Inorg. Chem.* **2015**, *54*, 3631 – 3642; l) S. K. Langley, C. M. Forsyth, B. Moubaraki, K. S. Murray, *Dalton Trans.* **2015**, *44*, 912 – 915; m) H. Li, W. Shi, Z. Niu, J. M. Zhou, G. Xiong, L. L. Lia, P. Chenga, *Dalton Trans.* **2015**, *44*, 468 – 471; n) L. Sun, H. Chen, C. Maa, C. Chen, *Dalton Trans.* **2015**, *44*, 20964 – 20971; o) X. Q. Song, P. P. Liu, Y.-A. Liu, J. J. Zhou, X. L. Wang, *Dalton Trans.* **2016**, *45*, 8154 – 8163; p) A. Gorczyński, M. Kubicki, D. Pinkowicz, R. Pełka, V. Patroniak, R. Podgajny, *Dalton Trans.* **2015**, *44*, 16833 – 16839; q) E. Colacio, J. Ruiz, E. Ruiz, E. Cremades, J. Krzystek, S. Carretta, J. Cano, T. Guidi, W. Wernsdorfer, E. K. Brechin, *Angew. Chem. Int. Ed.* **2013**, *52*, 9130 – 9134; *Angew. Chem.* **2013**, *125*, 9300 – 9304.

[7] a) S. Das, S. Hossain, A. Dey, S. Biswas, J. P. Sutter, V. Chandrasekhar, *Inorg. Chem.* **2014**, *53*, 5020 – 5028; b) S. Biswas, S. Das, J. V. Leusen, P. Kögerler, V. Chandrasekhar, *Dalton Trans.* **2015**, *44*, 19282 – 19293; c) S. Biswas, H. S. Jena, A. Adhikary, S. Konar, *Inorg. Chem.* **2014**, *53*, 3926 – 3928; d) V. Chandrasekhar, P. Bag, E. Colacio, *Inorg. Chem.* **2013**, *52*, 4562 – 4570; e) S. Goswami, A. Adhikary, H. S. Jena, S. Konar, *Dalton Trans.* **2013**, *42*, 9813 – 9817; f) J. Goura, J. P. S. Walsh, F. Tuna, V. Chandrasekhar, *Inorg. Chem.* **2014**, *53*, 3385 – 3391; g) S. Biswas, S. Das, J. v. Leusen, P. Kögerler, V. Chandrasekhar, *Eur. J. Inorg. Chem.* **2014**, 4159 – 4167; h) B. Joarder, A. K. Chaudhari, G. Rogez, S. K. Ghosh, *Dalton Trans.* **2012**, *41*, 7695 – 7699; i) S. Biswas, A. Mondal, S. Konar, *Inorg. Chem.* **2016**, *55*, 2085 – 2090; j) A. Mondal, V. S. Parmar, S. Biswas, S. Konar, *Dalton Trans.* **2016**, *45*, 4548 – 4557; k) A. K. Mondal, H. S. Jena, A. Malviya, S. Konar, *Inorg. Chem.* **2016**, *55*, 5237 – 5244; l) A. J. Calahorro, I. Oyarzabal, B. Fernández, J. M. Seco, T. Tian, D. F. Jimenez, E. Colacio, A. R. Diéguez, *Dalton Trans.* **2016**, *45*, 591 – 598; m) S. Biswas, S. Das, G. Rogez, V. Chandrasekhar, *Eur. J. Inorg. Chem.* **2016**, 3322 – 3329; n) J. Y. Ge, J. Ru, F. Gao, Y. Song, X. H. Zhouc, J. L. Zuo, *Dalton Trans.* **2015**, *44*, 15481 – 15490; o) G. Brunet, F. Habib, I. Korobkov, M. Murugesu, *Inorg. Chem.* **2015**, *54*, 6195 – 6202; p) K. H. Zangana, E. Moreno Pineda, R. E. P. Winpenny, *Dalton Trans.* **2015**, *44*, 12522 – 12525; q) L. Zhang, P. Zhang, L. Zhao, J. Wu, M. Guo, J. Tang, *Inorg. Chem.* **2015**, *54*, 5571 – 5578; r) A. Baniodeh, N. Magnani, S. Bräse, C. E. Anson, A. K. Powell, *Dalton Trans.* **2015**, *44*, 6343 – 6347; s) L. Zhang, P. Zhang, L. Zhao, J. Wu, M. Guoa, J. Tang, *Dalton Trans.* **2016**, *45*, 10556 – 10562.

[8] a) Y. N. Guo, G. F. Xu, P. Gamez, L. Zhao, S. Y. Lin, R. P. Deng, J. Tang, H. Zhang, *J. Am. Chem. Soc.* **2010**, *132*, 8538 – 8541; b) M. Yadav, A. Mondal, V. Mereacre, S. K. Jana, A. K. Powell, P. W. Roesky, *Inorg. Chem.* **2015**, *54*, 7846 – 7856; c) F. Pointillart, T. Guizouarn, B. Lefeuvre, S. Golhen, O. Cador, L. Ouahab, *Chem. Eur. J.* **2015**, *21*, 16929 – 16934; d) H. Ke, G. F. Xu, Y. N. Guo, P. Gamez, C. M. Beavers, S. J. Teatd, J. Tang, *Chem. Commun.* **2010**, *46*, 6057 – 6059; e) S. Y. Lin, L. Zhao, H. Ke, Y. N. Guo, J. Tang, Y. Guoa, J. Dou, *Dalton Trans.* **2012**, *41*, 3248 – 3252.

[9] S. Das, A. Dey, S. Biswas, E. Colacio, V. Chandrasekhar, *Inorg. Chem.* **2014**, *53*, 3417 – 3426.

[10] a) N. Randell, M. U. Anwar, M. W. Drover, L. N. Dawe, L. K. Thompson, *Inorg. Chem.* **2013**, *52*, 6731 – 6742; b) S. Xue, L. Zhao, Y. N. Guo, J. Tang, *Dalton Trans.* **2012**, *41*, 351 – 353.

[11] L. Zhang, P. Zhang, L. Zhao, S. Y. Lin, S. Xue, J. Tang, Z. Liu, *Eur. J. Inorg. Chem.* **2013**, 1351 – 1357.

[12] R. J. Blagg, L. Ungur, F. Tuna, J. Speak, P. Comar, D. Collison, W. Wernsdorfer, E. J. L. McInnes, R. E. P. Winpenny, *Nat. Chem.* **2013**, *5*, 673 – 678.

[13] Y. H. Chen, Y. F. Tsai, G. H. Lee, E. C. Yang, *J. Solid State Chem.* **2012**, *185*, 166 – 169.

[14] a) Y. Z. Zheng, Y. Lan, C. E. Anson, K. Annie, *Inorg. Chem.* **2008**, *47*, 10813 – 10815; b) S. Xue, L. Zhao, Y. N. Guo, R. Deng, Y. Guo, J. Tang, *Dalton Trans.* **2011**, *40*, 8347 – 8352; c) P. H. Guo, J. L. Liu, Z. M. Zhang, L. Ungur, L. F. Chibotaru, J.-D. Leng, F. S. Guo, M. L. Tong, *Inorg. Chem.* **2012**, *51*, 1233 – 1235; d) S. K. Langley, N. F. Chilton, I. A. Gass, B. Moubaraki, K. S. Murray, *Dalton Trans.* **2011**, *40*, 12656 – 12659; e) G. Abbas, Y. Lan, G. E. Kostakis, W. Wernsdorfer, C. E. Anson, A. K. Powell, *Inorg. Chem.* **2010**, *49*, 8067 – 8072; f) G. Abbas, G. E. Kostakis, Y. Lan, A. K. Powell, *Polyhedron* **2012**, *41*, 1 – 6; g) P.-H. Lin, T. J. Burchell, L. Ungur, L. F. Chibotaru, W. Wernsdorfer, M. Murugesu, *Angew. Chem. Int. Ed.* **2009**, *48*, 9489 – 9492; *Angew. Chem.* **2009**, *121*, 9653 – 9656; h) F. P. Yan, P. H. Lin, F. Habib, T. Aharen, M. Murugesu, Z. P. Deng, G. M. Li, W. B. Sun, *Inorg. Chem.* **2011**, *50*, 7059 – 7065; i) F. Luan, T. Liu, P. Yan, X. Zou, Y. Li, G. Li, *Inorg. Chem.* **2015**, *54*, 3485 – 3490; j) W. W. Kuang, L. L. Zhu, Y. Xu, P. P. Yang, *Inorg. Chem. Commun.* **2015**, *61*, 169 – 172; k) F. Luan, P. Yan, J. Zhu, T. Liu, X. Zoua, G. Li, *Dalton Trans.* **2015**, *44*, 4046 – 4053; l) S. Y. Lin, X. L. Li, H. Kec, Z. Xu, *CrystEngComm* **2015**, *17*, 9167 – 9174.

[15] a) L. Ungur, S. Y. Lin, J. Tang, L. F. Chibotaru, *Chem. Soc. Rev.* **2014**, *43*, 6894 – 6905; b) A. Soncini, L. F. Chibotaru, *Phys. Rev. B* **2008**, *77*, 220406 – 220410.

[16] a) T. Kaelberer, V. A. Fedotov, N. Papasimakis, D. P. Tsai, N. I. Zheludev, *Science* **2010**, *330*, 1510 – 1512; b) S. Xue, Y. N. Guo, L. Zhao, P. Zhanga, J. Tang, *Dalton Trans.* **2014**, *43*, 1564 – 1570.

[17] a) J. K. Tang, I. Hewitt, N. T. Madhu, G. Chastanet, W. Wernsdorfer, C. E. Anson, C. Benelli, R. Sessoli, A. K. Powell, *Angew. Chem. Int. Ed.* **2006**, *45*, 1729 – 1733; *Angew. Chem.* **2006**, *118*, 1761 – 1765; b) L. F. Chibotaru, L. Ungur, A. Soncini, *Angew. Chem. Int. Ed.* **2008**, *47*, 4126 – 4129; *Angew. Chem.* **2008**, *120*, 4194 – 4197; c) L. Ungur, W. Van den Heuvel, L. F. Chibotaru, *New J. Chem.* **2009**, *33*, 1224 – 1230; d) G. Novitchi, W. Wernsdorfer, L. F. Chibotaru, J. P. Costes, C. E. Anson, A. K. Powell, *Angew. Chem. Int. Ed.* **2009**, *48*, 1614 – 1619; *Angew. Chem.* **2009**, *121*, 1642 – 1647; e) S. Hans, *J. Phys. Condens. Matter* **2008**, *20*, 434201 – 434220.

[18] a) L. Ungur, S. K. Langley, T. N. Hooper, B. Moubaraki, E. K. Brechin, K. S. Murray, L. F. Chibotaru, *J. Am. Chem. Soc.* **2012**, *134*, 18554 – 18557; b) D. I. Plokhov, A. K. Zvezdin, A. I. Popov, *Phys. Rev. B* **2011**, *83*, 184415 – 184420.

[19] a) D. I. Plokhov, A. I. Popov, A. K. Zvezdin, *Phys. Rev. B* **2011**, *84*, 224436 – 224439; b) A. Soncini, L. F. Chibotaru, *Phys. Rev. B* **2010**, *81*, 132403 – 132406.

[20] K. Marinov, A. D. Boardman, V. A. Fedotov, N. Zheludev, *New J. Phys.* **2007**, *9*, 324 – 325.

[21] a) A. I. Popov, D. I. Plokhov, A. K. Zvezdin, *EPL* **2009**, *87*, 67004 – 67008; b) M. Trif, F. Troiani, D. Stepanenko, D. Loss, *Phys. Rev. Lett.* **2008**, *101*, 217201 – 217204.

[22] a) H. U. Güdel, U. Hauser, A. Furrer, *Inorg. Chem.* **1979**, *18*, 2730 – 2737; b) G. Amoretti, R. Caciuffo, S. Carretta, T. Guidi, N. Magnani, P. Santini, *Inorg. Chim. Acta* **2008**, *361*, 3771 – 3776.

[23] a) A. Bencini, D. Gatteschi, in *EPR of Exchange Coupled Systems*, Springer, Berlin, **1990**; b) A. L. Barra, D. Gatteschi, R. Sessoli, G. L. Abbati, A. Cornia, A. C. Fabretti, M. G. Uytterhoeven, *Angew. Chem. Int. Ed. Engl.* **1997**, *36*, 2329 – 2331; *Angew. Chem.* **1997**, *109*, 2423 – 2426.

[24] T. Gupta, G. Rajaraman, *J. Chem. Sci.* **2014**, *126*, 1569 – 1579.

[25] a) F. Aquilante, J. Autschbach, R. K. Carlson, L. F. Chibotaru, M. G. Delcey, L. De Vico, I. Fdez, N. Ferré, L. M. Frutos, L. Gagliardi, M. Garavelli, A. Giussani, C. E. Hoyer, G. L. Manni, H. Lischka, D. Ma, P. Å. Malmqvist, T. Müller, A. Nenov, M. Olivucci, T. B. Pedersen, D. Peng, F. Plasser, B. Pritchard, M. Reiher, I. Rivalta, I. Schapiro, J. Segarra-Martí, M. Stenrup, D. G. Truhlar, L. Ungur, A. Valentini, S. Vancoillie, V. Veryazov, V. P. Vysotskiy, O. Weingart, F. Zapata, R. Lindh, *J. Comput. Chem.* **2016**, *37*, 506 – 541; b) F. Aquilante, L. De Vico, N. Ferre, G. Ghigo, P. A. Malmqvist, P. Neogrady, T. B. Pedersen, M. Pitonak, M. Reiher, B. O. Roos, L. Serrano-Andres, M. Urban, V. Veryazov, R. Lindh, *J. Comput. Chem.* **2010**, *31*, 224 – 247; c) J. A. Duncan, *J. Am. Chem. Soc.* **2009**, *131*, 2416 – 2416; d) G. Karlström, R. Lindh, P. A. Malmqvist, B. O. Roos, U. Ryde, V. Veryazov, P. O. Widmark, M. Cossi, B. Schimmelpfennig, P. Neogrady, L. Seijo, *Comp. Mater. Sci.* **2003**, *28*, 222 – 239; e) V. Veryazov, P. O. Widmark, L. Serrano-Andres, R. Lindh, B. O. Roos, *Int. J. Quantum Chem.* **2004**, *100*, 626 – 635; f) L. Ungur, L. F. Chibotaru, http://www.molcas.org/documentation/manual/node95.html.

[26] L. Ungur, L. F. Chibotaru, POLY_ANISO program, KU Leuven, Belgium, **2007**.

[27] a) V. Chandrasekhar, S. Hossain, S. Das, S. Biswas, J. P. Sutter, *Inorg. Chem.* **2013**, *52*, 6346 – 6353; b) V. Chandrasekhar, S. Das, A. Dey, S. Hossain, J. P. Sutter, *Inorg. Chem.* **2013**, *52*, 11956 – 11965.

[28] a) S. Xue, L. Zhao, Y. N. Guo, P. Zhang, J. K. Tang, *Chem. Commun.* **2012**, *48*, 8946; b) Y. N. Guo, X. H. Chen, S. Xue, J. Tang, *Inorg. Chem.* **2011**, *50*, 9705.

[29] a) C. Kachi-Terajima, H. Miyasaka, A. Saitoh, N. Shirakawa, M. Yamashita, R. Clérac, *Inorg. Chem.* **2007**, *46*, 5861 – 5872; b) A. M. Ako, V. Mereacre,

I. J. Hewitt, R. Clerac, L. Lecren, C. E. Anson, A. K. Powell, *J. Mater. Chem.* **2006**, *16*, 2579 – 2586.

[30] G. Novitchi, G. Pilet, L. Ungur, V. V. Moshchalkov, W. Wernsdorfer, L. F. Chibotaru, D. Luneau, A. K. Powell, *Chem. Sci.* **2012**, *3*, 1169 – 1176.

[31] a) *Vogel's Textbook of Practical Organic Chemistry*, 5th ed. (Eds.: B. S. Furniss, A. J. Hannaford, P. W. G. Smith, A. R. Tatchell), ELBS, Longman, London, **1989**; b) D. B. G. Williams, M. Lawton, *J. Org. Chem.* **2010**, *75*, 8351 – 8354; c) X. Zeng, D. Coquiére, A. Alenda, E. Garrier, T. Prangé, Y. Li, O. Reinaud, I. Jabin, *Chem. Eur. J.* **2006**, *12*, 6393 – 6402.

[32] a) SMART & SAINT Software Reference manuals, Version 6.45, Bruker Analytical X-ray Systems, Inc., Madison, WI, **2003**; b) G. M. Sheldrick, SADABS, a software for empirical absorption correction, Ver. 2.05, University of Göttingen: Göttingen, Germany, **2002**; c) SHELXTL Reference Manual, Ver. 6.1, Bruker Analytical X-ray Systems, Inc., Madison, WI, **2000**; d) G. M. Sheldrick, SHELXTL, Ver. 6.12, Bruker AXS Inc., WI, Madison, **2001**; e) G. M. Sheldrick, *Acta Crystallogr. Sect. A* **2008**, *64*, 112 – 122; f) O. V. Dolomanov, L. J. Bourhis, R. J. Gildea, J. A. K. Howard, H. Puschmann, *J. Appl. Crystallogr.* **2009**, *42*, 339 – 341; g) Bradenburg, K. Diamond, Ver. 3.1eM, Crystal Impact GbR, Bonn, Germany, **2005**.

[33] B. O. Roos, R. Lindh, P. A. Malmqvist, V. Veryazov, P. O. Widmark, A. C. Borin, *J. Phys. Chem. A* **2008**, *112*, 11431 – 11435.

[34] B. Swerts, L. F. Chibotaru, R. Lindh, L. Seijo, Z. Barandiaran, S. Clima, K. Pierloot, M. F. A. Hendrickx, *J. Chem. Theory Comput.* **2008**, *4*, 586 – 594.

[35] P. A. Malmqvist, B. O. Roos, B. Schimmelpfennig, *Chem. Phys. Lett.* **2002**, *357*, 230 – 240.

[36] C. Das, S. Vaidya, T. Gupta, J. M. Frost, M. Righi, E. K. Brechin, M. Affronte, G. Rajaraman, M. Shanmugam, *Chem. Eur. J.* **2015**, *21*, 15639 – 15650.

[37] a) A. Bhunia, M. T. Gamer, L. Ungur, L. F. Chibotaru, A. K. Powell, Y. Lan, P. W. Roesky, F. Menges, C. Riehn, G. Niedner-Schatteburg, *Inorg. Chem.* **2012**, *51*, 9589 – 9597; b) L. F. Chibotaru, L. Ungur, C. Aronica, H. Elmoll, G. Pilet, D. Luneau, *J. Am. Chem. Soc.* **2008**, *130*, 12445 – 12455; c) H. L. C. Feltham, R. Clérac, L. Ungur, V. Vieru, L. F. Chibotaru, A. K. Powell, S. Brooker, *Inorg. Chem.* **2012**, *51*, 10603 – 10612; d) Y. N. Guo, G. F. Xu, W. Wernsdorfer, L. Ungur, Y. Guo, J. K. Tang, H. J. Zhang, L. F. Chibotaru, A. K. Powell, *J. Am. Chem. Soc.* **2011**, *133*, 11948 – 11951; e) X. C. Huang, V. Vieru, L. F. Chibotaru, W. Wernsdorfer, S. D. Jiang, X. Y. Wang, *Chem. Commun.* **2015**, *51*, 10373 – 10376; f) S. K. Langley, N. F. Chilton, L. Ungur, B. Moubaraki, L. F. Chibotaru, K. S. Murray, *Inorg. Chem.* **2012**, *51*, 11873 – 11881; g) S. K. Langley, L. Ungur, N. F. Chilton, B. Moubaraki, L. F. Chibotaru, K. S. Murray, *Chem. Eur. J.* **2011**, *17*, 9209 – 9218; h) S. K. Langley, L. Ungur, N. F. Chilton, B. Moubaraki, L. F. Chibotaru, K. S. Murray, *Inorg. Chem.* **2014**, *53*, 4303 – 4315; i) S. K. Langley, D. P. Wielechowski, V. Vieru, N. F. Chilton, B. Moubaraki, B. F. Abrahams, L. F. Chibotaru, K. S. Murray, *Angew. Chem. Int. Ed.* **2013**, *52*, 12014 – 12019; *Angew. Chem.* **2013**, *125*, 12236 – 12241; j) S. K. Langley, D. P. Wielechowski, V. Vieru, N. F. Chilton, B. Moubaraki, L. F. Chibotaru, K. S. Murray, *Chem. Sci.* **2014**, *5*, 3246 – 3256; k) S. K. Langley, D. P. Wielechowski, V. Vieru, N. F. Chilton, B. Moubaraki, L. F. Chibotaru, K. S. Murray, *Chem. Commun.* **2015**, *51*, 2044 – 2047; l) P. H. Lin, I. Korobkov, W. Wernsdorfer, L. Ungur, L. F. Chibotaru, M. Murugesu, *Eur. J. Inorg. Chem.* **2011**, 1535 – 1539; m) S. Y. Lin, W. Wernsdorfer, L. Ungur, A. K. Powell, Y.-N. Guo, J. Tang, L. Zhao, L. F. Chibotaru, H. J. Zhang, *Angew. Chem. Int. Ed.* **2012**, *51*, 12767 – 12771; *Angew. Chem.* **2012**, *124*, 12939 – 12943; n) J. L. Liu, F. S. Guo„ Z. S. Meng, Y. Z. Zheng, J. D. Leng, M.-L. Tong, L. Ungur, L. F. Chibotaru, K. J. Heroux, D. N. Hendrickson, *Chem. Sci.* **2011**, *2*, 1268 – 1272; o) J.-L. Liu, J. Y. Wu, Y. C. Chen, V. Mereacre, A. K. Powell, L. Ungur, L. F. Chibotaru, X. M. Chen, M. L. Tong, *Angew. Chem. Int. Ed.* **2014**, *53*, 12966 – 12970; *Angew. Chem.* **2014**, *126*, 13180 – 13184; p) V. S. Mironov, L. F. Chibotaru, A. Ceulemans, *J. Am. Chem. Soc.* **2003**, *125*, 9750 – 9760.

[38] M. E. Lines, *J. Chem. Phys.* **1971**, *55*, 2977 – 2984.

[39] K. S. Pedersen, J. Dreiser, H. Weihe, R. Sibille, H. V. Johannesen, M. A. Sørensen, B. E. Nielsen, M. Sigrist, H. Mutka, S. Rols, J. Bendix, S. Piligkos, *Inorg. Chem.* **2015**, *54*, 7600 – 7606.

Received: July 31, 2016